J. Fluid Mech. (2019), *vol.* 876, *pp.* 150–185. © Cambridge University Press 2019
doi:10.1017/jfm.2019.532

Optimal perturbations for controlling the growth of a Rayleigh–Taylor instability

Ali Kord[1,†] **and Jesse Capecelatro**[1]

[1]Department of Mechanical Engineering, University of Michigan, Ann Arbor, MI 48109-2125, USA

(Received 15 January 2019; revised 20 June 2019; accepted 27 June 2019;
first published online 31 July 2019)

A discrete adjoint-based method is employed to control multi-mode Rayleigh–Taylor (RT) instabilities via strategic manipulation of the initial interfacial perturbations. We seek to find to what extent mixing and growth can be enhanced at late stages of the instability and which modes are targeted to achieve this. Three objective functions are defined to quantify RT mixing and growth: (i) variance of mole fraction, (ii) a kinetic energy norm based on the vertical velocity and (iii) variations of mole fraction with respect to the unperturbed initial state. The sensitivity of these objective functions to individual amplitudes of the initial perturbations are studied at various stages of the RT instability. The most sensitive wavenumber during the early stages of the instability closely matches the most unstable wavenumber predicted by linear stability theory. It is also shown that randomly changing the initial perturbations has little effect at early stages, but results in large variations in both RT growth and its sensitivity at later times. The sensitivity obtained from the adjoint solution is employed in gradient-based optimization to both suppress and enhance the objective functions. The adjoint-based optimization framework was capable of completely suppressing mixing by shifting all of the interfacial perturbation energy to the highest modes such that diffusion dominates. The optimal initial perturbations for enhancing the objective functions were found to have a broadband spectrum resulting in non-trivial coupling between modes and depends on the particular objective function being optimized. The objective functions were increased by as much as a factor of nine in the self-similar late-stage growth regime compared to an interface with a uniform distribution of modes, corresponding to a 32% increase in the bubble growth parameter and 54% increase in the mixing width. It was also found that the interfacial perturbations optimized at early stages of the instability are unable to predict enhanced mixing at later times, and thus optimizing late-time multi-mode RT instabilities requires late-time sensitivity information. Finally, it was found that the optimized distribution of interfacial perturbations obtained from two-dimensional simulations was capable of enhancing the objective functions in three-dimensional flows. As much as 51% and 99% enhancement in the bubble growth parameter and mixing width, respectively, was achieved, even greater than what was reached in two dimensions.

Key words: instability control, variational methods

† Email address for correspondence: akord@umich.edu

https://doi.org/10.1017/jfm.2019.532 Published online by Cambridge University Press

1. Introduction

Turbulent mixing of variable-density flows is ubiquitous in nature and plays an important role in many engineering applications. Such examples include supernova explosions and neutron stars (Woosley & Weaver 1986; Fujimoto 1993; Janka & Müller 1996; Piro & Bildsten 2007), turbulent combustion (Peters 2000; Pitsch 2006, and references therein) and inertial confinement fusion (ICF) (Lindl 1995; Nakai & Takabe 1996). Turbulent mixing directly affects the overall performance of many engineering systems. For example, hydrodynamic instabilities that induce mixing decrease the efficiency of implosion performance in ICF (Lindl 1995; Nakai & Takabe 1996). Hydrodynamic mixing in ICF is thought to be controlled by Rayleigh–Taylor (RT) and Richtmyer–Meshkov instabilities originating from non-uniformities associated with irradiation laser intensity and the fuel target surface (Nakai & Takabe 1996). Control of RT-induced mixing is therefore of great importance to improve the performance of such devices.

Since the 1950s, a large number of theoretical (e.g. Chandrasekhar 1961; Duff, Harlow & Hirt 1962), numerical (e.g. Cook & Dimotakis 2001; Cabot & Cook 2006) and experimental (e.g. Read 1984; Roberts & Jacobs 2016) studies have provided a great deal of insight into the mixing properties of RT instabilities. In addition, several studies have been conducted to determine stabilizing or suppressing agents of RT growth, e.g. via shear rate and surface tension actions (Babchin *et al.* 1983), wall oscillations (Halpern & Frenkel 2001) and electric fields imposed on dielectric fluids (Cimpeanu, Papageorgiou & Petropoulos 2014). It has also been observed that the RT growth rate can be modified by altering the structure of initial interfacial perturbations (Cook & Dimotakis 2001; Ristorcelli & Clark 2004; Ramaprabhu, Dimonte & Andrews 2005; Banerjee & Andrews 2009; Youngs 2009; Xie *et al.* 2017), suggesting that one might be able to control the extent of fluid mixing by carefully adjusting the initial conditions. While such a strategy for manipulating fluid mixing might appear impractical in practice, it is interesting to note that Carles *et al.* (2006) and Huang *et al.* (2007) recently demonstrated that it is feasible to impose precise and arbitrary controlled initial perturbations using magnetic fields.

Several studies in the literature have examined the importance of initial perturbations on RT growth rates, yet it remains unclear to what extent details of the initial perturbations are retained throughout evolutionary stages of the instability. Many studies have shown that variations of initial interfacial perturbations in spectral space can affect the growth rate (e.g. Cook & Dimotakis 2001; Ristorcelli & Clark 2004; Ramaprabhu *et al.* 2005; Banerjee & Andrews 2009; Youngs 2009; Xie *et al.* 2017). For example, Banerjee & Andrews (2009) simulated several three-dimensional multi-mode RT configurations with different interfacial perturbation spectra, and obtained different growth rates in some cases. Xie *et al.* (2017) showed that it is possible to suppress or enhance growth by perturbing the amplitude of an individual mode of a two-dimensional multi-mode RT instability. In addition, it has been observed that including low wavenumber modes in the initial perturbations increases the late-time RT growth (Cook & Dimotakis 2001; Youngs 2003; Ramaprabhu *et al.* 2005; Banerjee & Andrews 2009). Despite the dependence of large-scale mixing and penetration on initial perturbations, it has been seen that small-scale features (e.g. molecular mixing) are usually less sensitive to the distribution of initial perturbations (Dimonte *et al.* 2004; Ramaprabhu *et al.* 2005; Banerjee & Andrews 2009). Contrary to these observations, some studies have shown that the RT growth rate can be insensitive to changes in initial interfacial perturbations (e.g. Livescu, Wei & Petersen 2011; Roberts & Jacobs 2016), especially if the growth is dominated by

https://doi.org/10.1017/jfm.2019.532 Published online by Cambridge University Press

nonlinear mode-coupling effects (e.g. Dimonte *et al.* 2004; Ramaprabhu *et al.* 2005; Banerjee & Andrews 2009).

Despite recent progress, practical methods to control mixing of multi-component fluids remain limited, and the extent to which instabilities can be altered remains an open question. In recent years, advancements in numerical methods and growing computational resources have enabled predictive simulations of realistic multi-component turbulent flows. Yet, the use of high-fidelity simulations for optimization in general remains challenging due to the high computational cost and large number of parameters capable of influencing mixing. In recent years, adjoint-based methods have emerged as a powerful technique to measure parametric sensitivity in fluid dynamic applications, including shape optimization and drag reduction for aerostructures (Jameson 1989; Jameson & Martinelli 2000; Martins, Alonso & Reuther 2004), sensitivity analysis of laminar flames (Braman, Oliver & Raman 2015), aeroacoustic control of free shear flows (Wei & Freund 2006; Vishnampet, Bodony & Freund 2015), scalar mixing (Vikhansky 2002; Liu 2006; Thiffeault 2012; Foures, Caulfield & Schmid 2014; Miles 2018; Vermach & Caulfield 2018) and hydrodynamic instability of lifted diffusion flames (Qadri, Chandler & Juniper 2015). Only recently have adjoint methods been applied to multi-component unsteady flows, including variable-density Kelvin–Helmholtz instabilities (Lopez-Zazueta, Fontane & Joly 2016) and turbulent combustion (Capecelatro *et al.* 2016; Capecelatro, Bodony & Freund 2017, 2018).

The sensitivity obtained from the adjoint solution can be susceptible to spatial and temporal truncation errors that are known to become significant in unsteady or chaotic flows (Lea, Allen & Haine 2000; Nadarajah & Jameson 2000; Vishnampet *et al.* 2015). Discrete adjoint methods address this by taking into account the numerical discretization prior to perturbing and linearizing the flow equations, which provides sensitivity that is exact up to machine round-off errors. Such an approach is expected accelerate and improve optimization for simulations of turbulence. For example, the discrete adjoint method has been shown to improve the minimum drag coefficient for flow around a rotating cylinder (Carnarius *et al.* 2010), and to achieve 2.2 $\times$ more reduction in aeroacoustic noise compared to the continuous adjoint approach (Vishnampet *et al.* 2015). Vishnampet *et al.* (2015) recently developed a discrete adjoint method for unsteady turbulent flows using high-order spatial and temporal discretization. In this work, we extend the space–time discrete adjoint approach of Vishnampet *et al.* (2015) to buoyancy-driven variable-density flows and measure sensitivity of multi-mode RT growth to local perturbations of the fluid interface. In § 2, the RT configuration, governing equations and discretization are presented. In § 3, different means for quantifying mixing are discussed, and the adjoint method is formulated for quantifying their sensitivity. Local sensitivity is analysed in § 4 at different times during the evolution of the instability. In § 5, the sensitivity obtained from the adjoint method is employed in gradient-based optimization to both suppress and enhance the growth rate, and the optimal perturbations associated with different RT regimes are evaluated.

2. Predictive model

2.1. *System configuration*

We consider two miscible fluids with molecular weight ratio $W_2/W_1 = 3$, corresponding to an Atwood number

$$At = \frac{W_2 - W_1}{W_2 + W_1} \tag{2.1}$$

https://doi.org/10.1017/jfm.2019.532 Published online by Cambridge University Press

of $At = 0.5$. The fluids are contained within a box of length $L \times 2L \times L$ with $L = 2\pi$. Gravity g is aligned in the negative y-direction. Periodic boundary conditions are imposed in the homogeneous x- and z-directions. A no-slip wall is enforced at the upper and lower boundaries, i.e. $y = \pm 2\pi$. The reference velocity is taken to be $u_\infty = \sqrt{gl}$ with the reference length scale $l = L/2\pi$, resulting in a Froude number $Fr = {u_\infty}^2/(gl) = 1$. The subscript ∞ denotes a reference quantity throughout the remainder of this paper.

The domain is discretized on a mesh with $256 \times 1025 \times 256$ grid points, corresponding to grid spacing $\Delta x = \Delta z = 0.025l$ in the horizontal directions and $\Delta y = 0.012l$ in the vertical direction. The average kinematic viscosity at the interface $\bar{\nu}$ is chosen such that the Kolmogorov length scale η is properly resolved, as determined by the Reynolds number

$$Re = \frac{u_\infty l}{\bar{\nu}} = \left(\frac{l}{\eta}\right)^{4/3}, \tag{2.2}$$

which is taken to be $Re = 353.3$ with $\eta = \Delta x/2$. The average kinematic viscosity is related to the light (μ_1) and heavy (μ_2) fluid viscosities via $\bar{\nu} = (\mu_1 + \mu_2)/(\rho_1 + \rho_2)$, where ρ_1 and ρ_2 are the densities of the fluid below and above the interface, respectively. The dynamic viscosity of the mixture, μ, is taken to be constant, i.e. $\mu = \mu_1 = \mu_2 = \mu_\infty$.

2.2. *Governing equations*

In this work, we consider the non-dimensional Navier–Stokes equations for a two-component fluid, given by

$$\frac{\partial \rho}{\partial t} + \frac{\partial \left(\rho u_j\right)}{\partial x_j} = 0, \tag{2.3}$$

$$\frac{\partial \left(\rho u_i\right)}{\partial t} + \frac{\partial}{\partial x_j}\left(\rho u_i u_j + p\delta_{ij}\right) = \frac{\partial \tau_{ij}}{\partial x_j} - \frac{\rho}{Fr_c}\delta_{2i}, \tag{2.4}$$

$$\frac{\partial \left(\rho E\right)}{\partial t} + \frac{\partial}{\partial x_j}\left[\left(\rho E + p\right) u_j\right] = -\frac{\partial q_j}{\partial x_j} + \frac{\partial \left(u_i \tau_{ij}\right)}{\partial x_j} - \frac{\rho u_2}{Fr_c}, \tag{2.5}$$

$$\frac{\partial \left(\rho Y\right)}{\partial t} + \frac{\partial \left(\rho u_j Y\right)}{\partial x_j} = \frac{1}{Re_c Sc}\frac{\partial^2 Y}{\partial x_j \partial x_j}, \tag{2.6}$$

for the non-dimensional conserved variables $\boldsymbol{Q} = [\rho\ \rho\boldsymbol{u}\ \rho E\ \rho Y]^{\mathrm{T}}$, where ρ is the mixture density, $\boldsymbol{u} = [u\ v\ w]^{\mathrm{T}}$ is the velocity vector, E is the total non-chemical energy (including thermal and kinetic energy), Y is the heavy fluid mass fraction with $1 - Y$ the mass fraction of the light fluid and p is the pressure given by

$$p = (\gamma - 1)\left(\rho E - \tfrac{1}{2}\rho u_i u_i\right), \tag{2.7}$$

where $\gamma = 1.4$ is the specific heat ratio. In (2.4)–(2.6), $Fr_c = Fr/Ma^2$ and $Re_c = Re/Ma$ denote the Froude and Reynolds numbers, respectively, based on the reference sound speed $c_\infty = \sqrt{\gamma p_I/\rho_I}$ with interfacial pressure p_I and density $\rho_I = (\rho_1 + \rho_2)/2$. The Mach number $Ma = u_\infty/c_\infty = 0.189$ is taken such that compressibility effects on the

https://doi.org/10.1017/jfm.2019.532 Published online by Cambridge University Press

RT instability are not important (Livescu 2004). The non-dimensional viscous stress tensor τ_{ij} is given by

$$\tau_{ij} = \frac{1}{Re_c}\left(\frac{\partial u_i}{\partial x_j} + \frac{\partial u_j}{\partial x_i} - \frac{2}{3}\frac{\partial u_k}{\partial x_k}\delta_{ij}\right), \tag{2.8}$$

and the non-dimensional heat flux is expressed as

$$q_i = -\frac{1}{Re_c Pr}\frac{\partial T}{\partial x_i} - \frac{T}{Re_c Sc}\left[\frac{1}{W_1}\frac{\partial (1-Y)}{\partial x_i} + \frac{1}{W_2}\frac{\partial Y}{\partial x_i}\right], \tag{2.9}$$

where T is the temperature that is determined by the ideal gas law for a mixture

$$T = \frac{\gamma p \overline{W}}{(\gamma - 1)\rho}, \tag{2.10}$$

where $\overline{W}$ denotes the mixture molecular weight, given by

$$\overline{W} = \left(\frac{Y}{W_2} + \frac{1-Y}{W_1}\right)^{-1}. \tag{2.11}$$

In (2.9), $Pr = C_{p,\infty}\mu/k$ is the Prandtl number with k and $C_{p,\infty}$ the thermal conductivity and reference specific heat at constant pressure, respectively, and $Sc = \mu/(\rho D)$ is the Schmidt number with mass diffusivity D. Values of $k/C_{p,\infty}$ and ρD are chosen to be constant such that $Pr = 0.7$ and $Sc = 1$.

2.3. *Initialization*

The mole fraction of the heavy fluid, $X = Y\overline{W}/W_2$, is initialized as

$$X = \frac{1}{2}\left\{1 + \mathrm{erf}\left[\frac{y - h_0(x,z)}{\delta_D}\right]\right\}, \tag{2.12}$$

where $\delta_D = 5\Delta y$ is the initial diffusion thickness of the interface, and $h_0(x,z)$ denotes the interfacial perturbations, composed of M modes in the x-direction and N modes in the z-direction, according to

$$h_0(x,z) = \sum_{m=1}^{M}\sum_{n=1}^{N} A_{m,n}\cos(k_{x,m}x + \theta_{x,m})\cos(k_{z,n}z + \theta_{z,n}). \tag{2.13}$$

Here, $k_{x,m} = 2\pi/\lambda_{x,m}$ and $k_{z,n} = 2\pi/\lambda_{z,n}$ are the perturbation wavenumbers with wavelengths $\lambda_{x,m}$ and $\lambda_{z,n}$ in x- and z-direction, respectively, with phase shift $\theta_{x,m}$ and $\theta_{z,n}$, and amplitude $A_{m,n}$.

The fluid is taken to be initially at rest, i.e. $u_i = 0$, and thus the momentum conservation equation (2.4) provides a hydrostatic relation for pressure, given by $\partial p/\partial y = -\rho/Fr_c$. Substituting ρ for p in the hydrostatic equation via (2.10) and integrating from $y = h_0(x,z)$ to an arbitrary vertical position y yields

$$p = p_I \exp\left(-\frac{\gamma}{(\gamma-1)T_0}\frac{1}{Fr_c} \times \left[\overline{W}(y - h_0) + \frac{\delta_D(W_2 - W_1)}{2\sqrt{\pi}}\left\{\exp\left[-\frac{(y-h_0)^2}{\delta_D^2}\right] - 1\right\}\right]\right). \tag{2.14}$$

https://doi.org/10.1017/jfm.2019.532 Published online by Cambridge University Press

Here, p_I is the fluid interface pressure and T_0 denotes the initial temperature that is assumed to be constant throughout the entire domain, resulting in an initially isothermal state. The density is initialized by substituting the resulting pressure into (2.10). It is important to note that employing stationary initial conditions with the hydrostatic pressure distribution $\partial p/\partial y = -\rho/Fr_c$ will generate spurious acoustic waves near the interface. These waves originate from pressure disturbances as a result of non-zero enthalpy diffusion that appears in the energy equation (Cook 2009; Livescu 2013; Reckinger, Livescu & Vasilyev 2016). Recent work has shown that the spurious waves can be suppressed by modifying the velocity field near the interface (Movahed 2014; Reckinger *et al.* 2016). In the current work, we follow a similar approach described by Reckinger *et al.* (2016) to eliminate these spurious oscillations, resulting in the following initial velocity

$$u_i = -\frac{1}{Re_c Sc}\frac{1}{\rho\overline{W}}\frac{\partial \overline{W}}{\partial x_i}. \tag{2.15}$$

2.4. *Discretization of the governing equations*

In the present work, spatial derivatives appearing in the governing equations (2.3)–(2.6) and (2.8)–(2.9) are obtained via a narrow-stencil finite difference operator that satisfies the summation-by-part (SBP) property (Kreiss & Scherer 1974; Strand 1994). We employ spatial derivatives with eighth-order accuracy in the interior domain and fourth order near the boundaries, resulting in fifth-order global accuracy. Second and mixed derivatives are obtained by applying the first derivative consecutively. Sixth-order SBP dissipation operators (Mattsson, Svärd & Nordström 2004; Vishnampet Ganapathi Subramanian 2015) are employed to damp spurious numerical waves that arise due to repeated first derivatives. The flow equations are integrated in time using a standard fourth-order Runge–Kutta scheme. A constant simulation timestep of $\Delta t = 2.67^{-4}\tau$ with $\tau = \sqrt{Fr_c L/lAt}$ a characteristic time scale is maintained such that the Courant–Friedrichs–Lewy (CFL) condition remains below $\mathrm{CFL} < 0.9$.

The SBP scheme is combined with the simultaneous-approximation-term (SAT) boundary treatment to ensure provable stability (Carpenter, Gottlieb & Abarbanel 1994; Svärd & Nordström 2008; Bodony 2010; Vishnampet Ganapathi Subramanian 2015). The SAT treatment is used to impose no-slip isothermal boundary conditions at $y = \pm 2\pi$ (Svärd & Nordström 2008; Vishnampet Ganapathi Subramanian 2015). In addition, absorbing sponge regions (Freund 1997) are applied near the walls by adding a damping term to suppress numerical acoustic waves and to enforce the solution to a target state $\boldsymbol{Q}_t$ (taken to be the unperturbed initial conditions). The damping term $\sigma_s(y)(\boldsymbol{Q} - \boldsymbol{Q}_t)$ is added to the right-hand side of the governing equations (2.3)–(2.6), where the sponge strength $\sigma_s(y)$ varies quadratically in the y-direction from unity at the walls to zero at $\approx 0.7l$ away from the wall.

3. Controlling the Rayleigh–Taylor instability

We seek to control RT growth by manipulating individual mode amplitudes $A_{m,n}$ of the initial perturbations at the fluid interface h_0, given by (2.13). Sensitivity of the instability with respect to each mode provides a direction that is useful in gradient-based optimization. In order to calculate this sensitivity, a quantitative measure of the RT instability is required. In this section, important features and concepts of RT growth are summarized. We then introduce various definitions of mixing that will be considered and provide a formal methodology for measuring its sensitivity to each individual amplitude $A_{m,n}$.

https://doi.org/10.1017/jfm.2019.532 Published online by Cambridge University Press

3.1. *A background on Rayleigh–Taylor growth*

RT instabilities are known to undergo a range of stages during their growth. In the limit that either the Schmidt number, the perturbation amplitude or gravity is sufficiently small, the initial growth will be dominated by diffusion (Duff *et al.* 1962; Cook & Dimotakis 2001; Wei & Livescu 2012). Following diffusional growth, the perturbation amplitude grows exponentially with time according to linear stability theory (Chandrasekhar 1961; Duff *et al.* 1962; Livescu 2004). The exponential growth holds when the perturbation amplitude h is significantly smaller than the perturbation wavelength λ, i.e. $h \ll \lambda$. When h is not sufficiently small, nonlinearities become important, and bubbles and spikes form as the two fluids penetrate each other, resulting in a growing mixing zone. During the nonlinear regime, the bubble tip velocity of a single-mode RT instability is known to reach a constant value proportional to $\sqrt{g\lambda}$ (Layzer 1955; Baker & Freeman 1981; Hecht, Alon & Shvarts 1994; Goncharov 2002). After sufficiently long time, the mixing zone grows quadratically (Anuchina *et al.* 1978; Youngs 1984), and the acceleration of bubbles and spikes becomes constant, given by (Read 1984; Youngs 1984)

$$h_{b/s}(t) = \alpha_{b/s} A t\, g t^2, \tag{3.1}$$

where indices 'b' and 's' denote bubbles and spikes, respectively, and α is the growth parameter. There are two primary mechanisms responsible for bubbles approaching self-similarity. The first mechanism, referred to as bubble competition, suggests that each ambient mode grows independently and exponentially until reaching its saturation limit, resulting in a set of saturated bubbles (Alon *et al.* 1994; Hecht *et al.* 1994; Dimonte 2004; Ramaprabhu *et al.* 2005; Banerjee & Andrews 2009). Such a mechanism results in a weak correlation between α_b and the amplitudes of the interfacial perturbations (Dimonte 2004; Ramaprabhu *et al.* 2005; Banerjee & Andrews 2009). The second mechanism, referred to as bubble merger, suggests that different bubbles merge and couple nonlinearly to create larger and faster bubbles (Sharp 1984; Alon *et al.* 1994; Dimonte 2004; Dimonte *et al.* 2004; Ramaprabhu *et al.* 2005; Banerjee & Andrews 2009). In contrast to bubble competition, the resulting α_b of pure mode coupling does not depend on initial perturbations (Alon *et al.* 1994; Dimonte *et al.* 2004; Ramaprabhu *et al.* 2005; Banerjee & Andrews 2009). Thus, no universal value for α exists, and a wide range of growth parameters have been reported from experiments and numerical simulations, ranging from $0.015 \lessapprox \alpha \lessapprox 0.085$ (Dimonte *et al.* 2004; Ramaprabhu *et al.* 2005). In order to more effectively control RT instabilities, it is important to identify to what extent α is influenced by the structure of the initial interfacial perturbations.

3.2. *Quantifying mixing*

In this work, the objective function, $\mathcal{J}$, is defined within the simulation domain $\mathbb{D}$ and time horizon $[0, t_f]$ as

$$\mathcal{J}(\boldsymbol{Q}, \boldsymbol{A}) = \int_0^{t_f} \int_{\mathbb{D}} \mathcal{I}(\boldsymbol{Q}, \boldsymbol{A}) \mathcal{W}(y)\, \mathrm{d}\boldsymbol{x}\, \mathrm{d}t, \tag{3.2}$$

where the integrand $\mathcal{I}$ denotes the local temporal mixing provided by a high-fidelity simulation that solves the governing equations (2.3)–(2.6), and $\boldsymbol{A} = [A_{1,1}, \ldots, A_{M,N}]^{\mathrm{T}}$.

https://doi.org/10.1017/jfm.2019.532 Published online by Cambridge University Press

The weighting function $\mathcal{W}(y)$ enforces compact support near the interface and smoothly decays to zero towards the vertical boundaries, given by

$$\mathcal{W}(y) = \tfrac{1}{2}\left\{\tanh\left[\sigma_{\mathcal{W}}\,(y+1-f_{\mathcal{W}}/2)\right] - \tanh\left[\sigma_{\mathcal{W}}\,(y-1+f_{\mathcal{W}}/2)\right]\right\}, \tag{3.3}$$

where $\sigma_{\mathcal{W}} = 25.0/l$ determines the slope, and $f_{\mathcal{W}} = 0.25l$ controls the fraction of the span for which $\mathcal{W}$ is maximum. The choice of these parameters have negligible effect on the results reported here.

The choice of $\mathcal{I}$ in (3.2) is critical for measuring mixing and growth of the RT instability. Several definitions for $\mathcal{I}$ can be found in the literature. One measure is the bubble–spike distance h_t (e.g. see Cook & Dimotakis 2001), given by

$$h_t = h_b - h_s. \tag{3.4}$$

For multi-mode RT instabilities, thresholds on spanwise-averaged mole, volume or mass fraction are typically used to measure bubble and spike heights (e.g. see Cook & Dimotakis 2001; Dimonte *et al.* 2004; Movahed 2014). In the present work, we consider $\langle X\rangle = 0.99$ and $\langle X\rangle = 0.01$ thresholds for determining bubble h_b and spike h_s heights, respectively, where $\langle\cdot\rangle$ denotes a spanwise average, given by

$$\langle\phi\rangle(y) = \frac{1}{L^2}\int_{-L/2}^{L/2}\int_{-L/2}^{L/2}\phi(x, y, z)\,\mathrm{d}z\,\mathrm{d}x, \tag{3.5}$$

where ϕ can be the mole, volume or mass fraction. Another common measure is the mixing width, given by (e.g. see Dimonte *et al.* 2004; Cabot 2006)

$$w = \int_{-L}^{L}\langle\phi\rangle\,(1-\langle\phi\rangle)\,\mathrm{d}y. \tag{3.6}$$

In addition, mixed fluid can be defined as the product of a hypothetical fast-kinetic reversible chemical reaction between two pure fluids, such that a corresponding mixing length is given by (e.g. see Cook & Dimotakis 2001; Movahed 2014)

$$h_m = \int_{-L}^{L}\phi_m\,(\langle\phi\rangle)\,\mathrm{d}y, \tag{3.7}$$

where h_m is the mixing height, and $\phi_m(\phi)$ is a corresponding mixed fluid fraction, where $\phi_m = 2\phi$ for $\phi \leqslant 0.5$; $\phi_m = 2\,(1-\phi)$ otherwise. In the current work, $\langle\phi\rangle = \langle X\rangle$ is considered in (3.6) and (3.7).

In the present work, the adjoint of the perturbed and linearized governing equations is solved to determine the sensitivity of mixing and growth, which requires the objective function to be differentiable with respect to flow variables $\boldsymbol{Q}$ and perturbation parameters $\boldsymbol{A}$. However, computing derivatives of the aforementioned quantities can be problematic, and thus necessitates a new measure of mixing. An initial candidate for $\mathcal{I}$ in (3.2) is to utilize the form of (3.6) with $\mathcal{I} = X\,(1-X)$, leading to $\mathcal{J}$ that quantifies mixing, defined as

$$\mathrm{MIX} = \int_0^{t_f}\int_{\mathbb{D}} X\,(1-X)\,\mathcal{W}(y)\,\mathrm{d}\boldsymbol{x}\,\mathrm{d}t, \tag{3.8}$$

https://doi.org/10.1017/jfm.2019.532 Published online by Cambridge University Press

in which its maximum value occurs at $X = 0.5$ (representing the fully mixed fluid), and $\mathrm{MIX} = 0$ within a pure fluid. It is important to note that due to the initial smooth distribution of X as given by (2.12), $\mathrm{MIX}(t = 0) \neq 0$ even for an unperturbed interface.

Alternatively, the definition of mixing can be defined based on the perturbation kinetic energy (Aamo, Krstić & Bewley 2003; Foures *et al.* 2014; Lopez-Zazueta *et al.* 2016; Vermach & Caulfield 2018). Because the interfacial fluid movement is closely related to the local velocity of the interface, it is reasonable to consider an L^2-norm of vertical velocity v, resulting in $\mathcal{J}$ that quantifies the kinetic energy, given by

$$\mathrm{KE} = \int_0^{t_f} \int_{\mathbb{D}} v^2 \mathcal{W}(y)\, \mathrm{d}\boldsymbol{x}\, \mathrm{d}t. \tag{3.9}$$

Foures *et al.* (2014) and Vermach & Caulfield (2018) showed that maximizing the perturbation kinetic energy does not effectively enhance mixing of a passive scalar in plane channel flows. Even so, the utility of this definition for controlling RT growth will be analysed in later sections.

In addition to the definitions above, we consider a third quantity that represents the deviation of mole fraction from its unperturbed initial value X_∞, according to

$$\mathrm{VAR} = \int_0^{t_f} \int_{\mathbb{D}} (X - X_\infty)^2\, \mathcal{W}(y)\, \mathrm{d}\boldsymbol{x}\, \mathrm{d}t, \tag{3.10}$$

where X_∞ is determined by (2.12) with $h_0(x, z) = 0$. VAR can be considered as the 'variance' of X with respect to the unperturbed field X_∞.

In the present work, we seek the sensitivity of these mixing quantities (3.8)–(3.10) with respect to the initial perturbation amplitude of each mode, $A_{m,n}$. Considering the variations of $\mathcal{J}$ with respect to $\boldsymbol{A}$, the sensitivity is given by the chain rule as

$$\frac{\delta \mathcal{J}}{\delta \boldsymbol{A}} = \frac{\partial \mathcal{J}}{\partial \boldsymbol{Q}} \frac{\delta \boldsymbol{Q}}{\delta \boldsymbol{A}} + \frac{\partial \mathcal{J}}{\partial \boldsymbol{A}}, \tag{3.11}$$

where δ denotes small variations. A brute-force approach for evaluating $\delta \boldsymbol{Q}/\delta \boldsymbol{A}$ would require perturbing each amplitude individually and performing a new simulation for each to measure the change in flow solution $\delta \boldsymbol{Q}$. In this work, that would require $M \times N$ solutions of the time-dependent multi-component Navier–Stokes equations, resulting in a prohibitively large number of simulations. An alternative, more computationally efficient approach is to solve the corresponding adjoint equations by linearizing the perturbed flow equations, which is addressed in the following section.

3.3. *Quantifying sensitivity of mixing*

The flow variables $\boldsymbol{Q}$ and initial perturbation amplitudes $\boldsymbol{A}$ are governed by the Navier–Stokes equations and its initial conditions, given by

$$\boldsymbol{\mathcal{M}}(\boldsymbol{Q}, \boldsymbol{A}) = \boldsymbol{\mathcal{N}}(\boldsymbol{Q}) + \left[\boldsymbol{Q}(\boldsymbol{A}) - \boldsymbol{Q}_0\right] \delta_{t=0} \equiv 0, \tag{3.12}$$

where $\boldsymbol{\mathcal{N}}$ denotes the flow equations (2.3)–(2.6), $\boldsymbol{Q}_0(\boldsymbol{A})$ are the flow variables at $t = 0$ and $\delta_{t=0}$ denotes the Dirac Delta function, which is unity for $t = 0$ and zero otherwise. The last term in (3.12) enforces the initial conditions and is presented as such to obtain the sensitivity of $\mathcal{J}$ to $\boldsymbol{A}$. A similar formulation can be found in Foures *et al.* (2014). The Lagrangian $\mathcal{L}$ of $\mathcal{J}$ constrained by $\boldsymbol{\mathcal{M}}$ is given by

$$\mathcal{L}(\boldsymbol{Q}, \boldsymbol{A}) = \mathcal{J}(\boldsymbol{Q}, \boldsymbol{A}) - \int_0^{t_f} \int_{\mathbb{D}} \boldsymbol{Q}^{\dagger \mathrm{T}} \boldsymbol{\mathcal{M}}(\boldsymbol{Q}, \boldsymbol{A})\, \mathrm{d}\boldsymbol{x}\, \mathrm{d}t, \tag{3.13}$$

https://doi.org/10.1017/jfm.2019.532 Published online by Cambridge University Press

where $\boldsymbol{Q}^\dagger = [\rho^\dagger\ \boldsymbol{u}^\dagger\ E^\dagger\ Y^\dagger]^{\mathrm{T}}$ with $\boldsymbol{u}^\dagger = [u^\dagger\ v^\dagger\ w^\dagger]^{\mathrm{T}}$ is the Lagrange multiplier, referred to here as the adjoint variable. Variations of $\mathcal{L}$ are expressed as

$$\begin{aligned}\delta\mathcal{L}(\boldsymbol{Q},\boldsymbol{A}) \;=\; \delta\mathcal{J}(\boldsymbol{Q},\boldsymbol{A}) - \int_0^{t_f}\int_{\mathbb{D}} \delta\boldsymbol{Q}^{\dagger\mathrm{T}}\boldsymbol{\mathcal{M}}(\boldsymbol{Q},\boldsymbol{A})\,\mathrm{d}\boldsymbol{x}\,\mathrm{d}t \\ - \int_0^{t_f}\int_{\mathbb{D}} \boldsymbol{Q}^{\dagger\mathrm{T}}\delta\boldsymbol{\mathcal{M}}(\boldsymbol{Q},\boldsymbol{A})\,\mathrm{d}\boldsymbol{x}\,\mathrm{d}t. \end{aligned} \tag{3.14}$$

The last two terms on the right-hand side of (3.14) are always zero according to (3.12), leading to $\delta\mathcal{L} = \delta\mathcal{J}$. Taking variations of $\delta\mathcal{J}$ and $\delta\mathcal{M}$ and substituting them into (3.14) yields

$$\begin{aligned}\delta\mathcal{J} \;=\; \int_0^{t_f}\int_{\mathbb{D}} \left[\left(\frac{\partial\mathcal{I}}{\partial\boldsymbol{Q}}\right)^{\mathrm{T}}\delta\boldsymbol{Q}\mathcal{W} - \boldsymbol{Q}^{\dagger\mathrm{T}}\delta\boldsymbol{\mathcal{N}} - \boldsymbol{Q}^{\dagger\mathrm{T}}\delta\boldsymbol{Q}\delta_{t=0}\right]\mathrm{d}\boldsymbol{x}\,\mathrm{d}t \\ + \int_0^{t_f}\int_{\mathbb{D}} \left[\left(\frac{\partial\mathcal{I}}{\partial\boldsymbol{A}}\right)^{\mathrm{T}}\mathcal{W} + \boldsymbol{Q}^{\dagger\mathrm{T}}\frac{\partial\boldsymbol{Q}_0}{\partial\boldsymbol{A}}\delta_{t=0}\right]\delta\boldsymbol{A}\,\mathrm{d}\boldsymbol{x}\,\mathrm{d}t, \end{aligned} \tag{3.15}$$

where $\delta\boldsymbol{\mathcal{N}}$ are variations of $\boldsymbol{\mathcal{N}}$ with respect to $\boldsymbol{Q}$. The adjoint variables $\boldsymbol{Q}^\dagger$ are chosen such that the first line of (3.15) vanishes, leading to the adjoint partial differential equations provided in appendix A. Putting this together, the sensitivity is computed as

$$\frac{\delta\mathcal{J}}{\delta\boldsymbol{A}} = \int_{\mathbb{D}} \boldsymbol{Q}_0^{\dagger\mathrm{T}}\frac{\partial\boldsymbol{Q}_0}{\partial\boldsymbol{A}}\,\mathrm{d}\boldsymbol{x} \quad \text{at } t=0. \tag{3.16}$$

To avoid measuring sensitivity near the domain boundaries, we multiply a weighting function, $\mathcal{W}_\Gamma$, with initial perturbation $h_0(x,z)$ that enforces compact support near the interface, and approaches zero towards the walls in a similar manner as (3.3). Therefore, the initial mole fraction equation (2.12) is modified according to

$$X = \frac{1}{2}\left\{1 + \mathrm{erf}\left[\frac{y - h_0(x,z)\mathcal{W}_\Gamma(y)}{\delta_D}\right]\right\}. \tag{3.17}$$

This modification does not significantly change the initial conditions provided that the weighting function is near unity in the vicinity of the interface and the imposed perturbation h_0 is small.

The sensitivity provided by the adjoint solution after discretizing (3.16) can induce truncation errors accumulated in $\boldsymbol{Q}^\dagger$ that may become significant in unsteady or chaotic flows (Nadarajah & Jameson 2000; Carnarius *et al.* 2010). Simulations of turbulent mixing like the ones considered here are particularly sensitive to this since the numerical resolution is often close to the limits of the discretization. To this end, the present work employs a discrete adjoint method that provides sensitivity with accuracy independent of the underlying numerical scheme and is only limited by machine-precision round-off error. This is achieved by considering the discrete counterpart of the inner product (3.2) and the fully discretized Navier–Stokes equations (in space and time) prior to employing the Lagrangian (3.13). Details of the space–time discrete adjoint formulation consistent with the SBP-SAT discretization outlined in § 2.4, and verification of its sensitivity gradient, can be found in Vishnampet *et al.* (2015), Capecelatro *et al.* (2018).

https://doi.org/10.1017/jfm.2019.532 Published online by Cambridge University Press

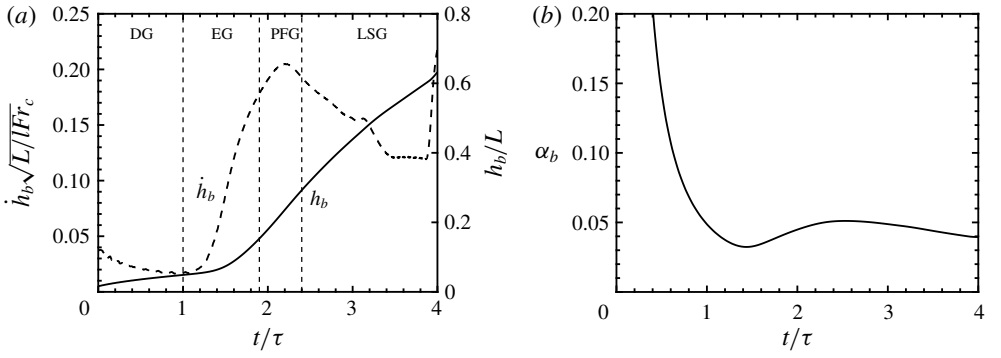


FIGURE 1. (*a*) Evolution of bubble height (–) and bubble tip velocity (––) of the three-dimensional RT instability through the diffusion growth (DG), exponential growth (EG), potential flow growth (PFG) and late-stage growth (LSG). (*b*) Corresponding bubble growth parameter α_b.

4. Sensitivity of a three-dimensional RT instability

4.1. *Rayleigh–Taylor growth*

In this section a three-dimensional multi-mode RT instability is considered. The interfacial amplitudes $A_{m,n}$ are initially distributed uniformly, i.e. $A_{m,n} = A_0$ for $m = 1, \ldots, M$ and $n = 1, \ldots, N$, and the phases are distributed randomly, $0 \leqslant \theta_{m,x}, \theta_{n,z} \leqslant 2\pi$. Thirty-two modes are considered in each horizontal direction (i.e. $M = N = 32$), and the smallest wavelength in each direction is $\lambda_{min} = 8\Delta x$. Linear stability theory predicts that the exponential growth rate of the incompressible ($p_I \to \infty$) RT instability is negative for $k > 21$ (Duff *et al.* 1962). Thus, the present configuration should account for all active modes. The root-mean-square (r.m.s.) of initial perturbation $h_{0,rms} = 3.15 \times 10^{-4} L$ is chosen based on Banerjee & Andrews (2009), which leads to $A_0 = 1.97 \times 10^{-5} L$.

The evolution of bubble height h_b and tip velocity $\dot{h}_b$ in figure 1(*a*) depict the various stages of RT growth up to $t = 4\tau$. The instability begins in the diffusion growth (DG) regime until $t \approx \tau$. Afterwards, gravitational effects become important, leading to the exponential growth (EG) regime until $t \approx 1.9\tau$. Then, nonlinearities become important, giving rise to a potential flow growth (PFG) stage where the bubble tip velocity is approximately constant until $t \approx 2.4\tau$. Afterwards, additional nonlinearities cause the bubble tip velocity to decrease. It then reaccelerates at $t \approx 3.9\tau$. The corresponding bubble growth parameter becomes approximately constant for $t > 2.5\tau$, where a self-similar late-stage growth (LSG) regime exists (see figure 1*b*). The bubble growth parameter is seen to approach $\alpha_b \approx 0.04$, consistent with values reported in the literature (e.g. Dimonte *et al.* 2004; Ramaprabhu *et al.* 2005). Two-dimensional snapshots of the mole fraction within different regimes do not show significant mixing until reaching the PFG stage (see figure 2).

The conventional measures for RT mixing, defined according to (3.4), (3.6) and (3.7), are compared with the objective functions defined in § 3.2 as given by (3.8)–(3.10) (see figure 3). Each quantity shows relatively small growth during the DG and EG stages, and a rapid increase in mixing after $t \approx 2\tau$, consistent with figures 1 and 2. It is interesting to note that the trend of each objective function is approximately similar. However, the growth of the kinetic energy norm KE (defined using $\mathcal{I} = v^2$) is seen to be delayed until $t \approx 2\tau$ due to diffusion effects. It then

https://doi.org/10.1017/jfm.2019.532 Published online by Cambridge University Press

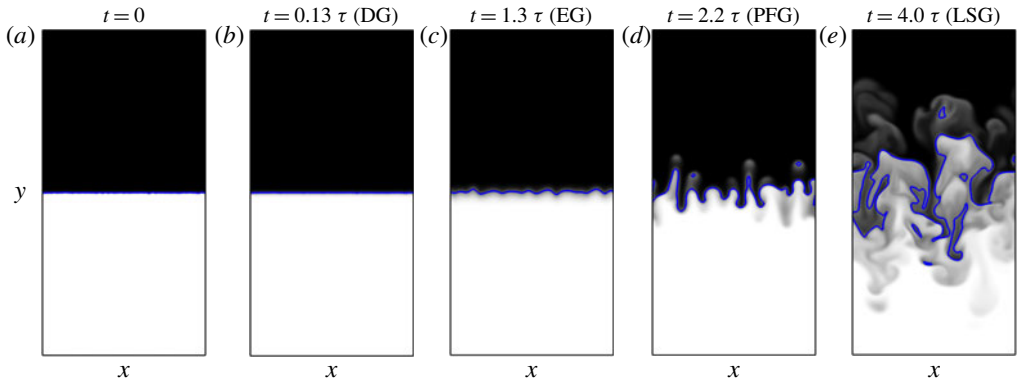


FIGURE 2. (Colour online) Evolution of mole fraction X in the $z=-\pi$ plane. The grey scale shows mole fraction from $X=0$ (white) to $X=1$ (black). The blue line depicts the fluid interface ($X=0.5$).

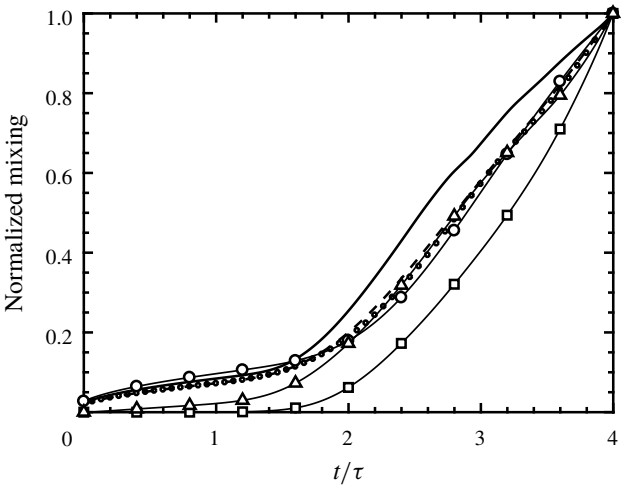


FIGURE 3. Conventional measures for RT mixing: h_t (–), w (– –) and h_m (· · ·). Instantaneous values of the objective functions MIX (–○–), KE (–□–) and VAR (–△–). All data are normalized by their final values (at $t=4\tau$).

increases exponentially according to linear stability theory during the EG regime ($t \gtrapprox 1.6\tau$). Both MIX (defined using $\mathcal{I} = X(1-X)$) and the mixing width w are observed to evolve in a similar manner, which is not unexpected due to their similarities in definition. The initial growth of bubble–spike distance h_t is similar to that of the mixing height, mixing width and MIX. This suggests the objective functions presented in § 3.2 act as good surrogates for quantifying RT growth and mixing. Sensitivity of these quantities to the initial interfacial perturbations will be presented in the following section.

4.2. *Sensitivities to different measures of mixing*

The sensitivity of $\mathcal{J}$ to $\boldsymbol{A}$ over duration t_f are evaluated across the averaged perturbation wavenumbers $k=\sqrt{k_x^2+k_z^2}$ (see figure 4). It can immediately be seen that

https://doi.org/10.1017/jfm.2019.532 Published online by Cambridge University Press

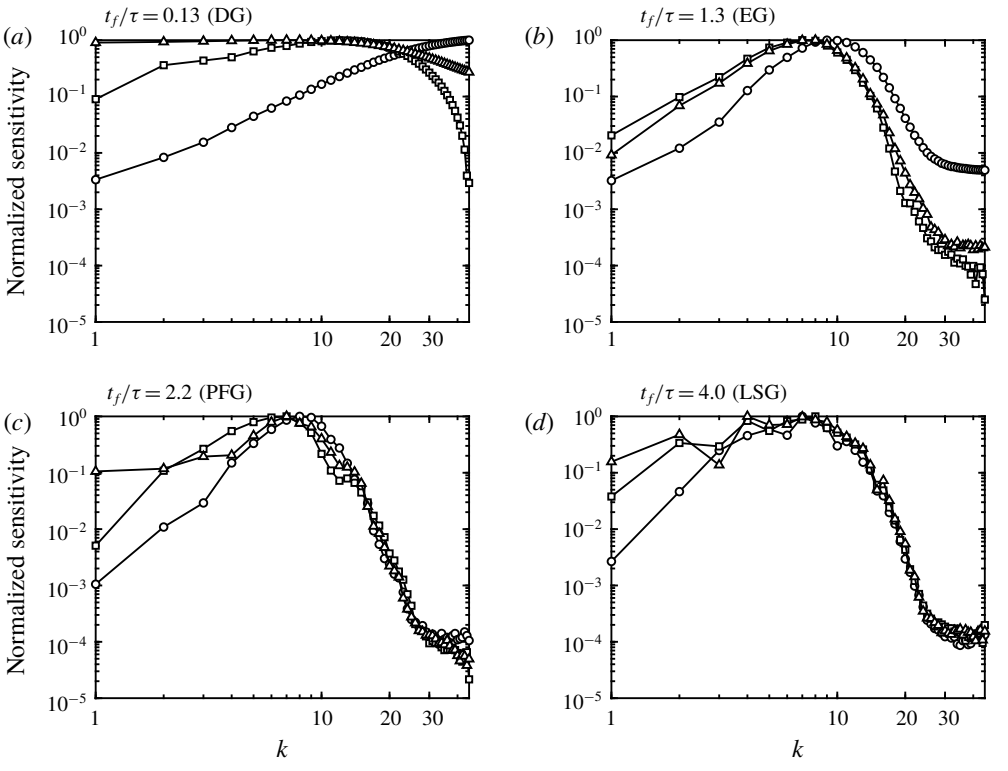


FIGURE 4. Magnitude of sensitivity $|\delta\mathcal{J}/\delta\boldsymbol{A}|$ integrated over different durations t_f for MIX (–○–), KE (–□–) and VAR (–△–). The sensitivities are shown as a function of initial perturbation wavenumber $k = \sqrt{k_x^2 + k_z^2}$ and normalized by their corresponding maximum value.

at early stages of the RT instability the distribution of sensitivity varies between the different quantities of interest, and collapse at late time. Within the DG stage, VAR and KE are most sensitive to low and intermediate wavenumber perturbations, and are least sensitive at the highest wavenumbers (see figure 4*a*). Perhaps surprisingly, MIX exhibits an opposite trend, with sensitivity increasing with increasing k. This suggests that when diffusion dominates, the largest changes to the quantity $X(1-X)$ can be achieved by perturbing the perturbation amplitude at the highest wavenumbers. This early-time behaviour can be predicted analytically by assuming the mole fraction evolves according to a diffusion equation. Assuming purely diffusional growth, the distribution of sensitivity with k can be shown to be a consequence of the functional dependence of $\mathcal{J}$ on X and initial conditions. A detailed comparison of the theoretical estimates of early-time sensitivity and the adjoint solution for each objective function is provided in appendix B.

Inertial effects from buoyancy become more significant as time increases. Linear stability theory predicts that the exponential growth rate within the EG regime, $\sigma_k^{(EG)}$, is given by (Duff *et al.* 1962)

$$\sigma_k^{(EG)} = \left[\frac{At\,k}{\psi Fr_c} + \frac{k^4}{\rho_I^2 Re_c^2}\right]^{1/2} - \left(1 + Sc^{-1}\right)\frac{k^2}{\rho_I Re_c}, \tag{4.1}$$

https://doi.org/10.1017/jfm.2019.532 Published online by Cambridge University Press

where ψ depends on the Atwood number, wavenumber and the thickness of the diffusive layer (see Duff *et al.* 1962). The above relation predicts $k = 7.58$ as the most unstable wavenumber at $t = 0$. As shown in figure 4(*b*), this is consistent with the most sensitive wavenumber provided by the adjoint solution in the EG regime. As the time duration increases, the most sensitive modes corresponding to MIX shifts from the highest wavenumbers to lower ones. Within the PFG and LSG regimes, the distribution of sensitivity is similar for all objective functions, with maximum sensitivity remaining close to the most unstable wavenumber predicted by linear stability theory. Except for MIX in the DG regime, the objective functions are generally unaffected by perturbation modes at wavenumbers $k > 20$. Linear stability theory predicts that these modes are damped by diffusion during the EG regime.

It is interesting to note that the most sensitive wavenumber throughout the growth of the RT instability remains approximately constant and consistent with the most unstable wavenumber predicted by linear stability theory. However, its distribution varies. This suggests that employing linear stability theory for manipulating growth of the instability may have only limited success due to the broadband nature of sensitivity. This will be confirmed in § 5.

It is important to note that the sensitivity obtained by the adjoint solution in chaotic dynamic systems is known to diverge when measured over long time horizons (e.g. see Lea *et al.* 2000; Wang & Gao 2013). Thus, the values used for normalization in figure 4 will change depending on the duration considered. Following Wang & Gao (2013), its chaotic behaviour is characterized by estimating the first Lyapunov exponent, Λ, for the adjoint solution of each objective function over the duration $t_f = 4.0\tau$, according to

$$\left\| \sum_{i=1}^{6} Q_i^\dagger(\boldsymbol{x}, t)\mathcal{W}_\Gamma(y) \right\|_2 \propto \exp(-\Lambda t), \tag{4.2}$$

where $\|\cdot\|_2$ is a spatial L^2 norm operator, and $i = 1, \ldots, 6$ denotes the ith component of adjoint variable. The value of Λ estimates the average growth rate in $\delta\mathcal{J}$ due to small changes in initial interfacial perturbations (e.g. see Trevisan & Legnani 1995). As can be seen in figure 5, the magnitude of the adjoint variables exponentially increase in inverse time with rates $\Lambda = 3.42\tau^{-1}$, $3.48\tau^{-1}$ and $3.45\tau^{-1}$ for MIX, KE and VAR, respectively. From this, the rate at which sensitivity diverges does not significantly differ among the different objective functions. We note that the positive first Lyapunov exponents of each objective function limits the time horizon that can be considered, which may affect the optimization of the instability during late-time growth. The utility of the adjoint solution for controlling the RT instability will be addressed in § 5.3. The next section will analyse local sensitivity at various stages of the instability.

4.3. *Spatial sensitivity at various stages of the RT instability*

In this section we evaluate the spatial distribution of sensitivity at different stages of the instability. The sensitivity gradient defined in (3.16) can be rewritten as

$$\frac{\delta\mathcal{J}}{\delta\boldsymbol{Q}_0} = \int_{\mathbb{D}} \int_0^{t_f} \frac{\delta\mathcal{I}}{\delta\boldsymbol{Q}_0} \,\mathrm{d}t\,\mathrm{d}\boldsymbol{x} = \int_{\mathbb{D}} \boldsymbol{Q}_0^\dagger \,\mathrm{d}\boldsymbol{x}. \tag{4.3}$$

https://doi.org/10.1017/jfm.2019.532 Published online by Cambridge University Press

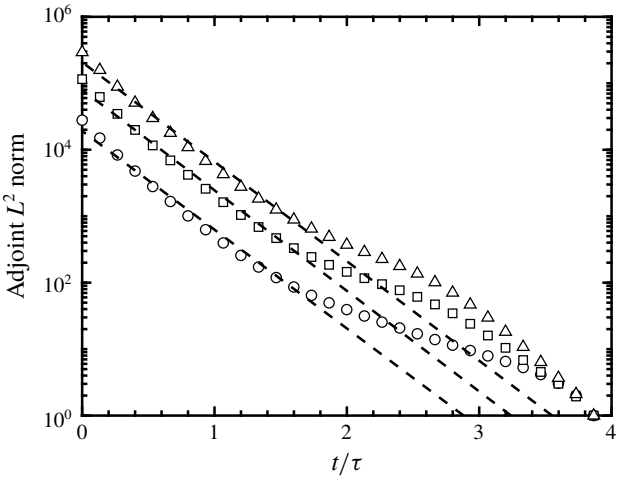


FIGURE 5. The L^2 norm of adjoint solutions for MIX (○), KE (□) and VAR (△). The L^2 norms are normalized by the corresponding values at $t = 3.87\tau$. The dashed lines estimate the growth in the adjoint solution based on the first Lyapunov exponent, which was found to be $\Lambda = 3.42\tau^{-1}$, $3.48\tau^{-1}$ and $3.45\tau^{-1}$ for MIX, KE and VAR, respectively.

Thus, the local adjoint variables $Q_i^\dagger$ at $t = 0$ provide spatial sensitivity of the mixing norms to the flow state. With this, the local sensitivity of $\mathcal{J}$ with respect to initial mole fraction variations can be expressed as

$$\frac{\delta \mathcal{J}}{\delta X_0} = \rho Y^\dagger \frac{\partial Y}{\partial X}, \tag{4.4}$$

where the chain rule is used, and $\partial Y/\partial X$ can be determined using the relation $Y = XW_1/W$.

The spatial distribution of $\delta\mathcal{J}/\delta X_0$ for VAR integrated over different durations in the vertical plane $z = -\pi$ are compared in figures 6(*a*)–6(*d*) and at the fluid interface $X = 0.5$ in figures 6(*e*)–6(*h*). As can be seen in figures 6(*a*)–6(*d*), local sensitivity exhibits a periodic distribution that is maximum near the interface. As was shown in the previous section, the dominant wavenumber of local sensitivity at the interface during the EG stage corresponds to $k \simeq 7$, consistent with the most unstable wavenumber mode predicted by liner stability theory (see figure 6*f*). Local sensitivity does not significantly change from EG to PFG (see figure 6*g*). However, the sensitivity in the LSG stage exhibits more variations near the interface, suggesting a broader range of modes contribute to mixing. Figures 6(*e*)–6(*h*) show that adjusting the perturbations at the fluid interface could both locally increase (positive sensitivity) or decrease (negative sensitivity) the mixing norm. Non-uniformities in sensitivity observed at the *x*–*z* plane suggest that the effects of spatial variations in the initial conditions on mixing persist at late time stages of the growth.

4.4. *The role of initial conditions on late-time sensitivity*

In the previous sections we considered initial interfacial perturbations with uniform amplitude and random phase. In order to evaluate the effects of initial perturbations on different stages of the RT growth, phases $\theta_{x,m}$ and $\theta_{z,n}$ are varied while holding

https://doi.org/10.1017/jfm.2019.532 Published online by Cambridge University Press

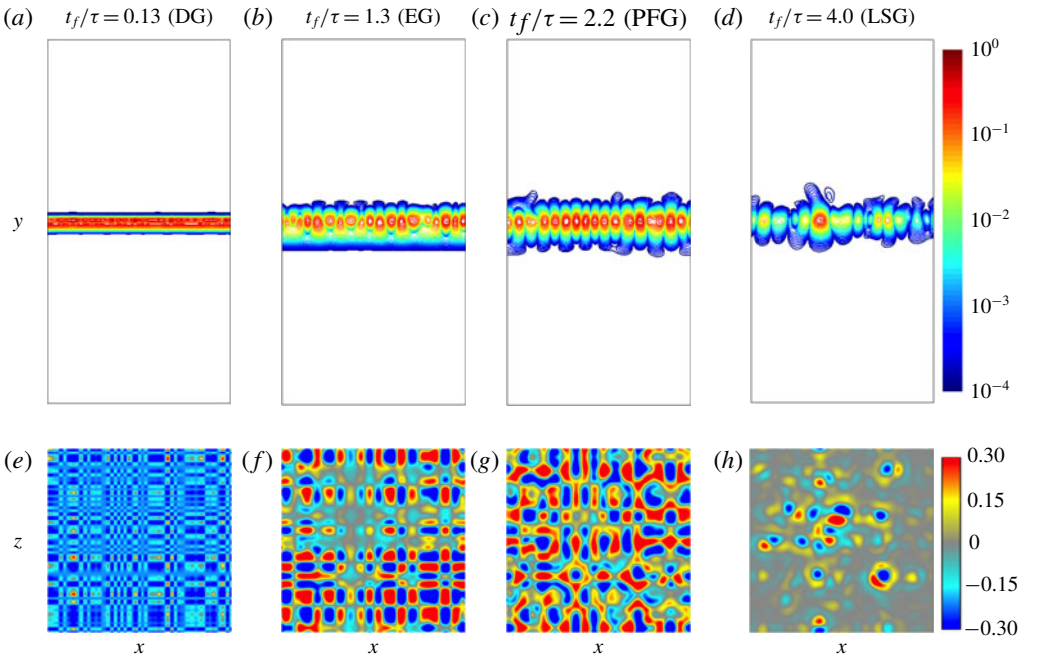


FIGURE 6. (Colour online) Normalized sensitivities of VAR to initial mole fraction ($\delta\mathcal{J}/\delta X_0$) in physical space for different time durations $t \in [0, t_f]$. The sensitivities are normalized by their maximum value. (*a–d*) Normalized sensitivity magnitude at $z = -\pi$. (*e–h*) Normalized sensitivity at the fluid interface ($X = 0.5$).

the amplitudes constant. Haan (1989) showed that a group of perturbation modes with similar phases can regionally combine and create a net perturbation amplitude during an RT instability. Thus, we expect that changing the initial perturbation phases while holding the initial amplitudes constant should lead to different nonlinear growth. The evolution of $\dot{h}_b$, α_b and $\mathcal{I} = (X - X_\infty)^2$ with different initial random phases are compared in figure 7. The bubble growth during the DG and EG stages is insensitive to the initial random phases, while deviations appear during the PFG and LSG regimes (see figure 7*a*). The bubble tip velocity corresponding to one of the realization decelerates following a PFG state, and later reaccelerates. On the other hand, another realization exhibits a reacceleration regime after PFG, prior to deceleration. Another realization exhibits a long PFG regime, with a slight deceleration in the bubble growth rate α_b while the other illustrates a combination of short-time accelerations and decelerations during the LSG regime. A chaotic behaviour is observed during the LSG regime. Meanwhile, it can be seen that the bubble growth parameter α_b marginally changes for these initial conditions (see figure 7*b*). In addition, the objective function $\mathcal{I} = (X - X_\infty)^2$ corresponding to different initial phases is similar until $t \approx 2\tau$ at which point it diverges (see figure 7*c*).

Figure 7 shows that the growth is insensitive to initial random phases until $t \approx 2\tau$. For each k, the sensitivity averaged over all realizations during early ($t_f = 2.2\tau$) and late ($t_f = 4.0\tau$) nonlinear stages is shown in figure 8. It can be seen that randomly adjusting the phases leads to significant variations in sensitivity at late stages. A set of modes $2 \leqslant k \leqslant 10$ is highly sensitive to initial phases when $t_f = 2.2\tau$ (see figure 8*a*). At later times, a broader range of modes are sensitive to the initial phases (see figure 8*b*).

https://doi.org/10.1017/jfm.2019.532 Published online by Cambridge University Press

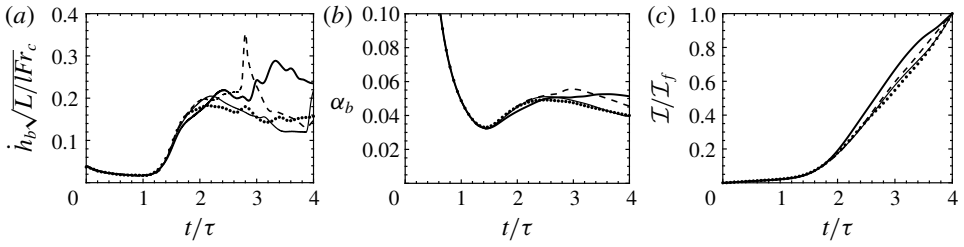


FIGURE 7. Evolution of (*a*) the bubble tip velocity, (*b*) bubble growth parameter and (*c*) instantaneous objective function VAR ($\mathcal{I} = (X - X_\infty)^2$), for four different initial interfacial perturbations of the three-dimensional RT instability.

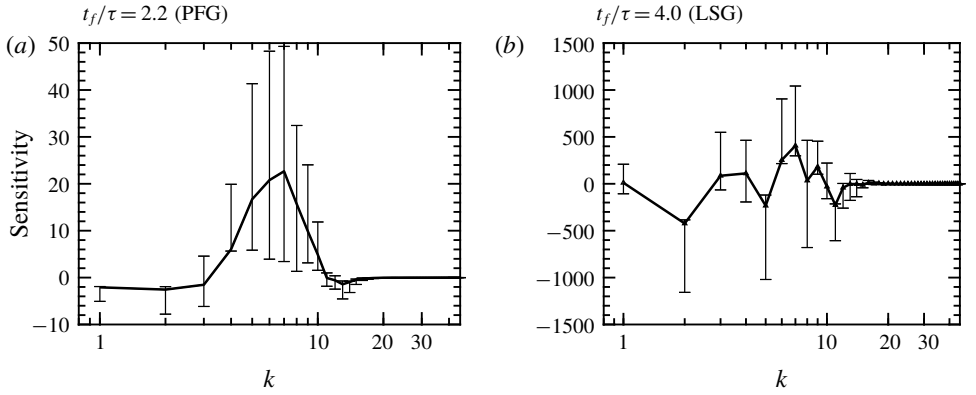


FIGURE 8. Ensemble-averaged sensitivities of VAR ($\delta\mathcal{J}/\delta\boldsymbol{A}$) for different random initial phases. The sensitivities are shown as a function of initial perturbation wavenumber $k = \sqrt{k_x^2 + k_z^2}$. The vertical bars illustrate the minimum and maximum sensitivities at each wavenumber.

This is consistent with the positive values of the first Lyapunov exponent discussed in § 4.2 (see figure 5).

5. Optimizing a two-dimensional RT instability

In the previous section, the sensitivity of multi-mode three-dimensional RT instabilities was analysed. The sensitivity $\delta\mathcal{J}/\delta\boldsymbol{A}$ provides the direction towards which the objective function increases (or decreases) with changes to each individual amplitude. In this section, the sensitivity obtained from the adjoint solution is employed in a gradient-based optimization framework in order to seek the optimal interfacial perturbations for suppressing and enhancing mixing during the growth of the RT instability. Despite the increased efficiency in computing the sensitivity provided by the adjoint, a direct numerical simulation of three-dimensional multi-mode RT instabilities remains computationally demanding. Thus, optimization of the three-dimensional RT instability would be limited to a small number of iterations. To this end, optimization is performed in two dimensions, with all other parameters considered in § 4 kept unchanged. Therefore, only the perturbation amplitudes A_m and phases $\theta_{x,m}$ are varied. In addition, the same r.m.s. of initial perturbation $h_{0,rms} = 3.15 \times 10^{-4}L$ is considered. The baseline solution has a uniform distribution

https://doi.org/10.1017/jfm.2019.532 Published online by Cambridge University Press

of perturbation energy across all wavenumbers, corresponding to an initial amplitude for each mode $A_0 = 7.875 \times 10^{-5}L$.

The optimization procedure can be summarized as

$$\begin{aligned} \text{minimize/maximize} \quad & \mathcal{J}(A_m, \boldsymbol{Q}(A_m)), \\ \text{with respect to} \quad & A_m, \quad m = 1, \ldots, M, \\ \text{subject to} \quad & \sum_{m=1}^{M} A_m^2 = \text{const.}, \\ & |A_m| \leqslant 4.5 \times 10^{-4} L. \end{aligned} \tag{5.1}$$

The constraint $\sum_{m=1}^{M} A_m^2$ enforces the perturbation energy to be constant, preventing a trivial solution (e.g. $A_m = 0$ or $A_m \gg A_0$). Keeping the perturbation energy constant also provides an upper bound for each amplitude. This bound is imposed on the amplitudes to constrain the optimizer. The amplitudes can take negative values which are interpreted as changes in perturbation phase $\theta_{x,m}$. The optimization procedure (5.1) is solved by a sequential least squares programming (SLSQP) algorithm (Kraft 1988) that leverages the `SciPy minimize` package, an open source Python library (Jones *et al.* 2001; Oliphant 2007; Millman & Aivazis 2011). The tolerance for termination is set to 10^{-6}. The objective function, constraint and gradients are taken as inputs to the optimization library that enforces the amplitude bounds of (5.1).

5.1. *Selectively assigning the perturbation energy*

Before performing the optimization, two-dimensional simulations of RT instabilities are reported with carefully chosen interfacial perturbations for comparison in later sections. As discussed in § 4, perturbations with wavenumbers $k > 21$ are suppressed during the EG stage according to linear stability theory (Duff *et al.* 1962). Therefore, it is expected that the optimized solution for minimizing RT mixing corresponds to an interface with all of the energy contained in the highest wavenumbers, leading to pure diffusional growth. Yet, the optimized solution for enhancing mixing is less obvious. In the context of scalar mixing, it is well known that large flow structures are controlled by advection while small length scales are mainly mixed by diffusion (e.g. see Foures *et al.* 2014; Miles 2018). For RT instabilities, it has been observed that assigning more perturbation energy into low wavenumber modes increases the growth parameter α (e.g. see Cook & Dimotakis 2001; Ristorcelli & Clark 2004; Banerjee & Andrews 2009; Youngs 2009). In addition, Cook & Dimotakis (2001) showed that seeding the lowest wavenumbers leads to 'the largest unmixedness'. In summary, it is expected that increased bubble/spike penetration occurs when more perturbation energy is added to low wavenumbers of the initial interface. When the perturbations are distributed among the highest wavenumber modes mixing is dominated by diffusion.

With this in mind, three different initial conditions are considered: (i) a uniform distribution of modal energy with random phases (similar to the configuration used § 4) serving as the baseline solution for the remainder of the paper; (ii) all the energy contained in the lowest wavenumber denoted here as Case A; and (iii) all the energy contained in the highest wavenumber referred to here as Case B. As shown in figure 9, the baseline case yields bubble and spike penetration associated with low perturbation wavenumbers as well as diffusion mixing associated with high wavenumbers. Nonlinear mode coupling also occurs due to the existence of high

https://doi.org/10.1017/jfm.2019.532 Published online by Cambridge University Press

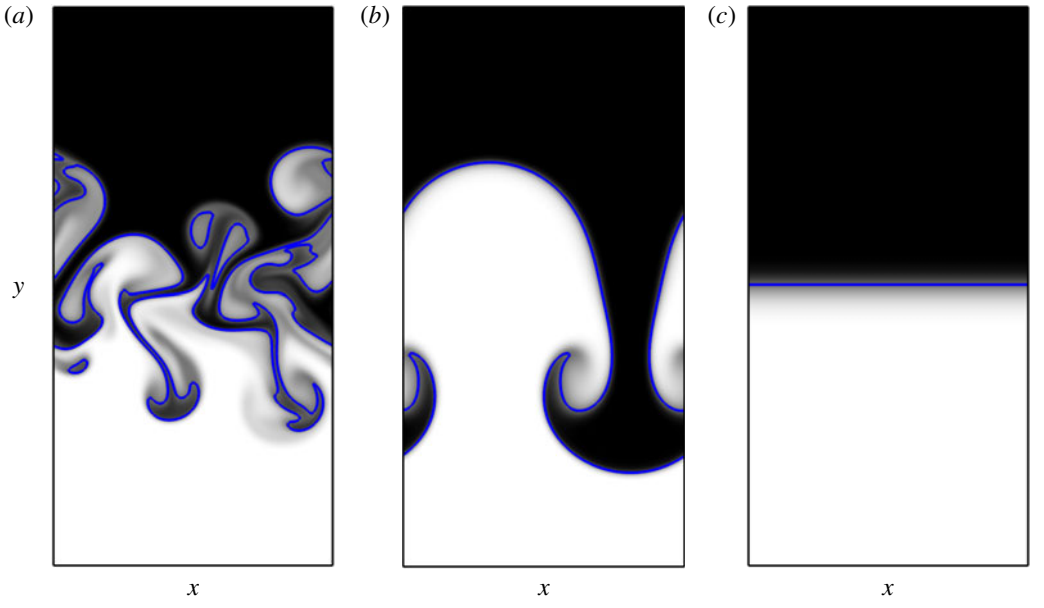


FIGURE 9. (Colour online) Bubble and spike structures of a two-dimensional RT instability at $t = 4.0\tau$ with different initial interfacial perturbations. (*a*) Baseline (uniform amplitude among all wavenumbers), (*b*) Case A (all energy contained in the lowest mode) and (*c*) Case B (all energy contained in the largest mode). Same colour scheme as figure 2.

wavenumber interfacial perturbations. Case A produces large amounts of penetration through the formation of a bubble and spike. The interfacial perturbation is suppressed in Case B during early-time regimes according to linear stability theory (Duff *et al.* 1962), and mixing is dominated by diffusion throughout the duration of the simulation.

Values of the corresponding objective functions for the three cases are reported in table 1. Both the lowest and highest wavenumber distributions produce smaller MIX values compared to the uniform distribution. The corresponding integrand, $\mathcal{I} = X(1 - X)$, is maximum for completely mixed fluid ($X = 0.5$) and zero for pure fluids. Thus, neither single-mode case produces as much mixing as in the uniform case as a result of nonlinear mode coupling. Case A demonstrates solely large-scale fluid penetration, resulting in high interfacial velocity and thus larger values of KE compared the other objective functions. Assigning the initial perturbation energy into the lowest mode increases KE by almost a factor of 2 compared to the baseline case. Comparatively, putting all the perturbation energy into the highest wavenumber decreases KE by 5 orders of magnitude due to dissipation of kinetic energy by diffusion. Putting all the energy into the lowest mode increases VAR by almost 30 % compared to the baseline case. The largest possible value of the VAR integrand, $\mathcal{I}_\infty = (X - X_\infty)^2$, occurs when the two fluids are inverted (i.e. the light fluid on top and heavy fluid on bottom). Thus, larger values of VAR occur in the presence of fluid penetration rather than pure mixing.

Figure 10 shows a comparison of the bubble height, bubble tip velocity and mixing width of the two-dimensional RT instability with the three different initial conditions. The bubble tip velocity in Case A approaches the PG regime at a later time compared to the baseline case due to the baseline case containing energy in modes with greater

https://doi.org/10.1017/jfm.2019.532 Published online by Cambridge University Press

Normalized objective function	Case A	Case B	$\min_{A_m} \mathcal{J}(\boldsymbol{Q}, A_m)$	$\max_{A_m} \mathcal{J}(\boldsymbol{Q}, A_m)$
MIX	0.432	0.397	0.397	1.386
KE	1.987	5.13×10^{-5}	6.70×10^{-5}	8.853
VAR	1.266	0.075	0.075	3.111

TABLE 1. Objective functions measured over duration $t_f = 4.0\tau$ normalized by their baseline solution $\mathcal{J}^{(0)}$ (uniformly distributed perturbation energy).

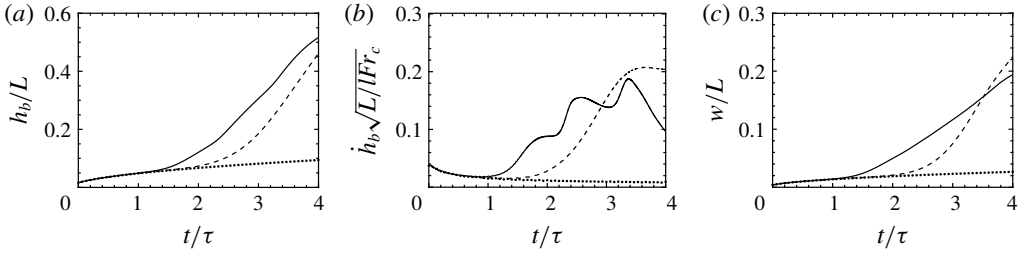


FIGURE 10. Evolution of (*a*) bubble height, (*b*) bubble tip velocity and (*c*) mixing width of the two-dimensional RT instability with different initial interfacial perturbation energy: baseline (–), Case A (– –) and Case B (· · ·).

exponential growth rate. In addition, nonlinear mode-coupling effects absent in Case A and Case B result in increased growth. The EG stage holds while $h_0 \ll \lambda$, and thus Case A will not exceed the EG regime until a greater time interval has passed compared with the baseline case. In contrast, the bubble tip velocity of Case B decreases due to diffusion.

Finally, it can be seen that the two-dimensional multi-mode RT instability (figures 9 and 10) grows more slowly compared to the three-dimensional flow (figures 1 and 2). This is consistent with previous work that shows how three-dimensional RT instabilities grow faster than their two-dimensional counterparts during the early nonlinear regime (Layzer 1955; Hecht *et al.* 1994; Oron *et al.* 2001; Goncharov 2002). This is due to reduced kinematic drag associated with three-dimensional bubbles compared to elongated two-dimensional bubbles, leading to a greater terminal bubble tip velocity in three dimensions.

5.2. *Optimal solution for suppressing mixing*

As discussed in the previous section, we expect mixing and growth to be suppressed by transferring all of the perturbation energy into the highest wavenumber modes such that diffusion dominates. In this section, this solution is sought by minimizing the objective functions via the gradient-based optimization method described earlier. Figure 11(*a*) shows the value of each objective function during the iterative process of the optimization procedure. Different levels of reduction are observed for each objective function. The optimized quantities are listed in table 1. Adjoint-based optimization is capable of reducing KE and VAR by more than an order of magnitude compared to their baseline values while MIX is only reduced by approximately 60 %. Due to the initially smooth distribution of mole fraction as defined in (2.12), MIX will remain finite even in the absence of any mixing or growth. As a consequence, its optimal solution approaches the value from Case B and not zero. As expected, the

https://doi.org/10.1017/jfm.2019.532 Published online by Cambridge University Press

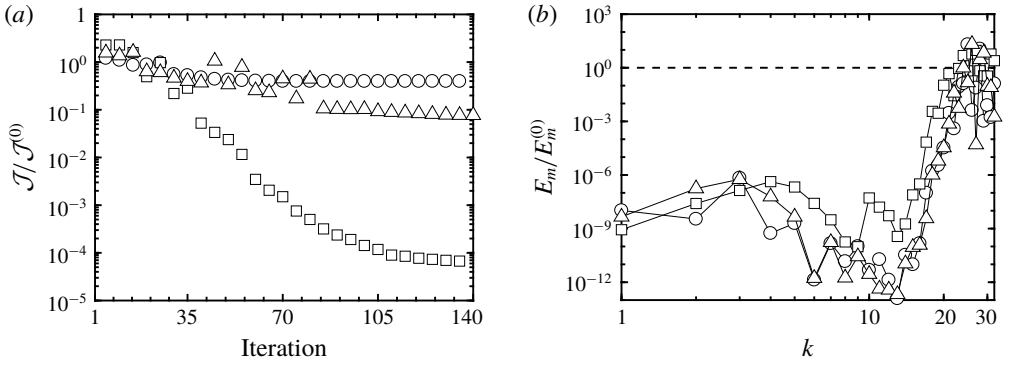


FIGURE 11. (*a*) Reduction of the objective functions normalized by their corresponding baseline values $\mathcal{J}^{(0)}$ for MIX (○), KE (□) and VAR (△). (*b*) The spectrum of interfacial perturbation energy for the baseline case (– –) and the optimized solution (symbols).

perturbation energy of the optimized solution for each objective function is transferred to high wavenumber modes, resulting in diffusion dominated growth (see figure 11*b*).

5.3. *Optimal solution for enhancing mixing*

Based on previous studies of multi-mode RT instabilities (e.g. see Cook & Dimotakis 2001; Ristorcelli & Clark 2004; Banerjee & Andrews 2009; Youngs 2009), it is anticipated that maximizing late-time growth requires shifting the perturbation energy towards the low wavenumber modes. In this section, we seek the optimal distribution of modal energy that enhances the three objective functions with respect to the baseline case denoted by $\mathcal{J}^{(0)}$ – an interface with uniform amplitude and random phase. It should be noted that gradient-based optimization provides a local extremum and there is no guarantee that such a solution holds globally. To this end, different initial configurations were considered as the starting point in the optimization process. The optimized spectra reported here correspond to an initial distribution of modal energy that was found to produce the greatest changes in $\mathcal{J}$.

The iteration history of the three objective functions shows that MIX is increased by approximately 40 %, KE by 900 % and VAR by 300 % (see table 1 and figure 12*a*). The initial interfacial perturbation energy of the three enhanced solutions indicates that low wavenumber modes have a greater contribution to RT growth and mixing (see figure 12*b*). It can be seen that the majority of perturbation energy of the high wavenumber modes is transferred to the first five wavenumbers. The optimized solutions exhibit non-trivial mode competition and coupling effects that enhance mixing. Nonlinear mode coupling generates lower wavenumber modes that move faster in the flow during the potential regime. Mode coupling also creates high wavenumber modes that are diminished by molecular diffusion. These effects are reflected in the optimized initial perturbations shown in figure 12(*b*), especially for the objective functions that measure the fluid penetration and growth, i.e. KE and VAR. It can be seen that the perturbation energy sharply decreased for $k > 21$, where the exponential growth rate is expected to be negative according to linear stability theory.

The optimized solutions at $t = 4.0\tau$ for KE and VAR exhibit greater fluid penetration compared to the baseline case, while MIX appears qualitatively to be more mixed (see

https://doi.org/10.1017/jfm.2019.532 Published online by Cambridge University Press

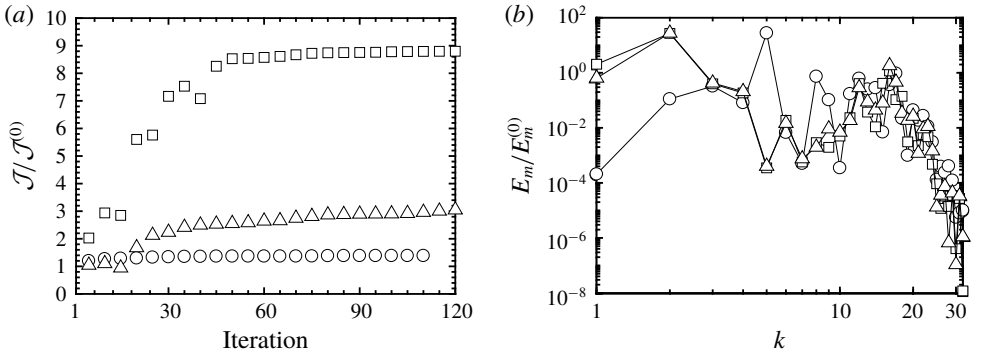


FIGURE 12. (*a*) Enhancement of the objective functions over duration $t_f = 4\tau$ normalized by their corresponding baseline values $\mathcal{J}^{(0)}$ for MIX (○), KE (□), and VAR (△). (*b*) The spectrum of initial interfacial perturbation energy of the optimized solution.

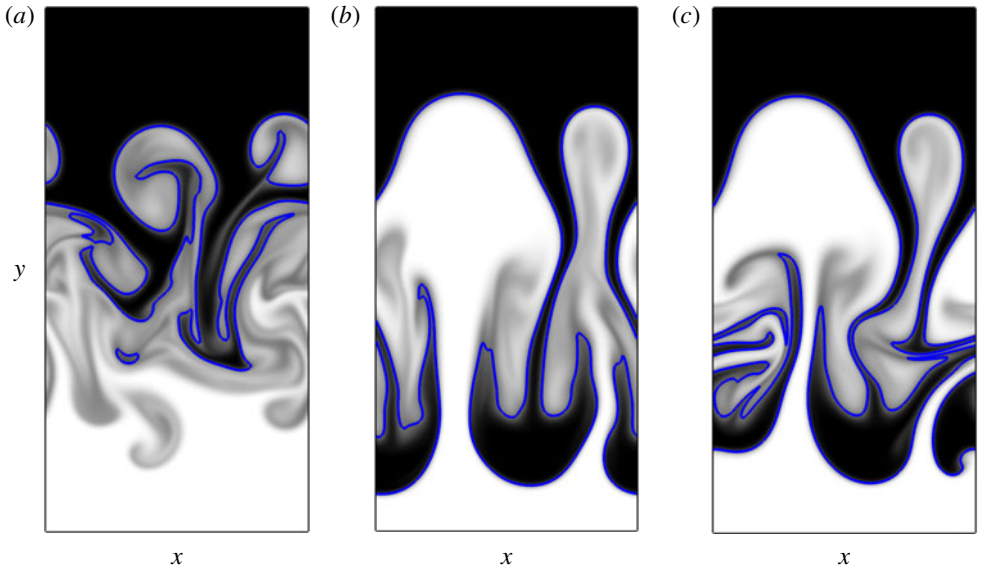


FIGURE 13. (Colour online) Mole fraction at $t = 4.0\tau$ of the optimized solution for enhancing the three objective functions (*a*) MIX, (*b*) KE and (*c*) VAR. Compared to the baseline case, MIX, KE and VAR are enhanced by factors of 1.4, 8.9 and 3.1, respectively. Same colour scheme as figure 2.

figure 13). The optimized solutions admit enhancement in conventional measures for RT mixing as well (see figure 14). The values of α_b at $t = 4\tau$ are increased by 17 %, 32 % and 31 %, with respect to the baseline case for MIX, KE and VAR, respectively. The mixing width w was also increased by as much as 54 % compared with the baseline case. It is notable that although $k \approx 8$ corresponds to the most, according to linear stability theory, unstable wavenumber and is thus the fastest growing mode during the EG stage, a single-mode initial perturbation of $k = 8$ is not sufficient to optimize growth at later times.

https://doi.org/10.1017/jfm.2019.532 Published online by Cambridge University Press

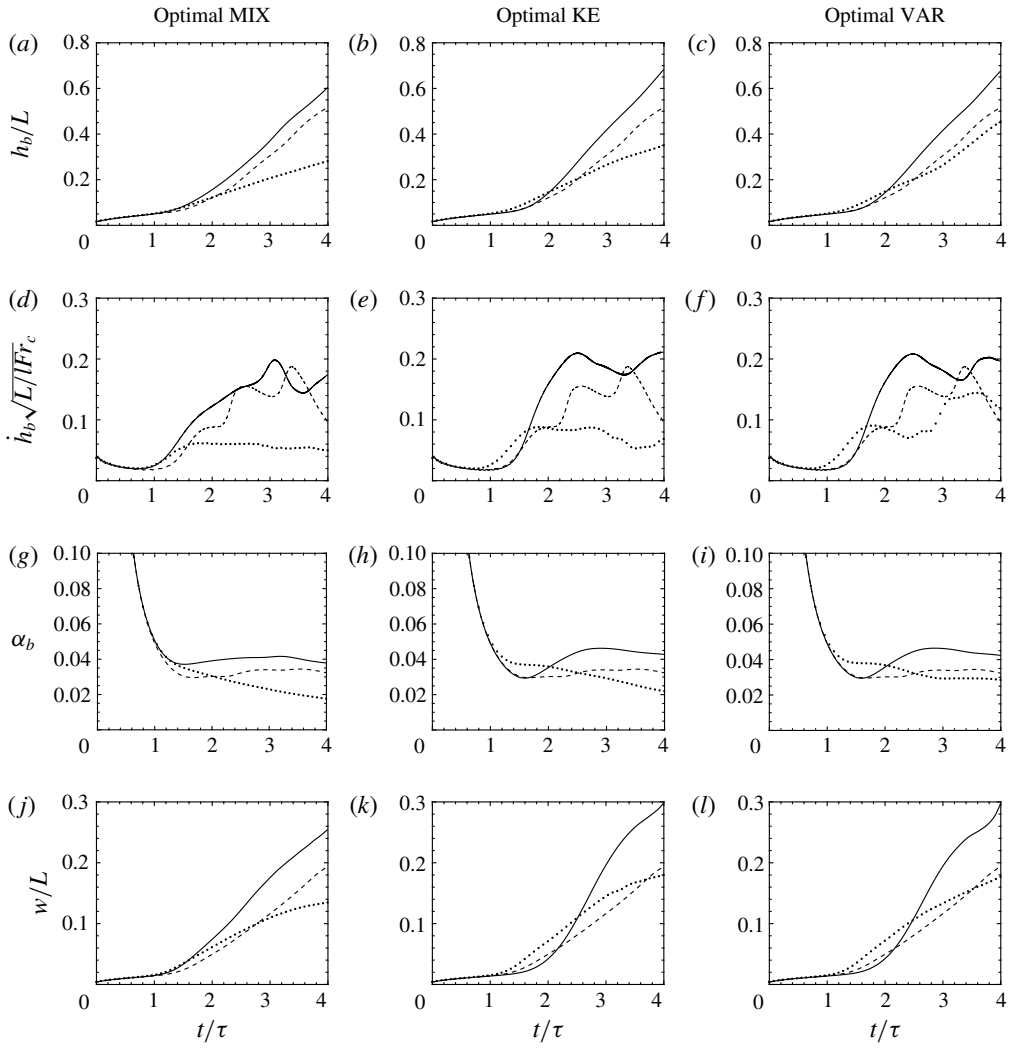


FIGURE 14. Evolution of (*a–c*) bubble height, (*d–f*) bubble tip velocity, (*g–i*) bubble growth parameter and (*j–l*) mixing width of the uniform distribution solution (– –), from the optimized solution over duration $t_f = 2\tau$ $(\cdots)$ and $t_f = 4\tau$ (–).

The effect of the time duration over which the objective function is computed (t_f) on enhancing mixing is also studied. The optimization of the three forms of $\mathcal{J}$ over duration $t_f = 2\tau$ is performed. At this stage of the instability the bubble tip velocity was observed to saturate due to nonlinearities (see figure 10*b*). Evolution of RT growth (h_b, $\dot{h}_b$ and α_b) and mixing width w corresponding to the optimal values of $\mathcal{J}$ over duration $t_f = 2\tau$ are compared with the baseline case and the enhanced values over duration $t_f = 4\tau$ (see figure 14). While the optimized $t_f = 2\tau$ solutions predict larger values for some of the quantities when $t < 2\tau$, they are found to be suboptimal when $t \gtrsim 2\tau$ compared to the solutions optimized for $t_f = 4\tau$. Interestingly, the initial perturbations optimized for $t_f = 2\tau$ were found to be suboptimal compared to the baseline solution when $t \gtrsim 2\tau$ as well. For the baseline case, low wavenumber initial perturbations and nonlinear mode-coupling effects augment RT growth at later

https://doi.org/10.1017/jfm.2019.532 Published online by Cambridge University Press

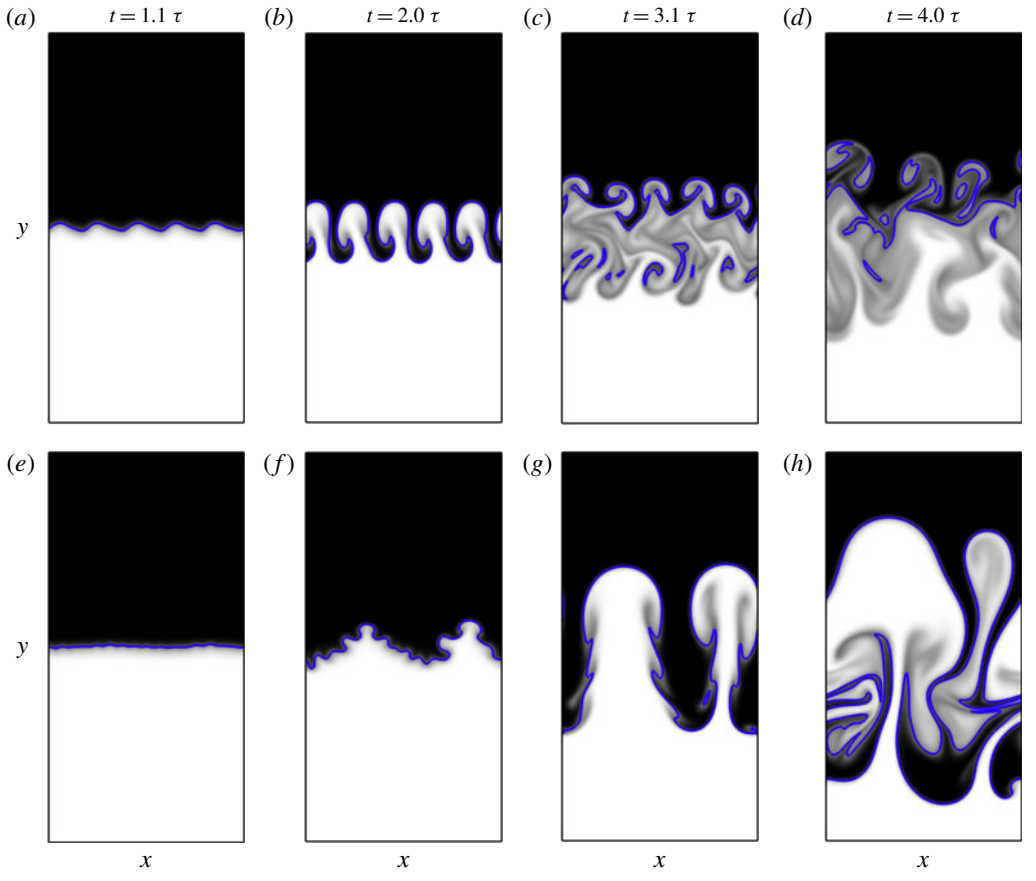


FIGURE 15. (Colour online) Evolution of mole fraction using the optimized perturbation amplitudes that maximize VAR over duration (*a–d*) $t_f = 2\tau$ and (*e–h*) $t_f = 4\tau$. Same colour scheme as figure 2.

times, while they are not as present in the optimal $t_f = 2\tau$ solutions. These differences become more obvious by observing the evolution of the mole fraction of optimal VAR for $t_f = 2\tau$ and $t_f = 4\tau$ (see figure 15). Initially, there is more fluid penetration in the optimal $t_f = 2\tau$ solution as the initial perturbation assigns more energy to wavenumbers close to the most unstable mode predicted by linear stability theory. However, at later times, the lower wavenumber modes grow faster. These results indicate that optimization of late-time stages of RT instabilities requires late-time sensitivity information.

5.4. *Enhancing three-dimensional mixing using optimal two-dimensional perturbations*

Here we evaluate the ability to enhance mixing of a three-dimensional RT instability using the optimal interfacial perturbations determined from the two-dimensional simulations in § 5.3. The initial perturbation energy shown in figure 12(*b*) is used to initialize the three-dimensional configuration presented in § 4. The optimized amplitudes A_m in two dimensions are transformed into $A_{m,n}$ in three dimensions by

https://doi.org/10.1017/jfm.2019.532 Published online by Cambridge University Press

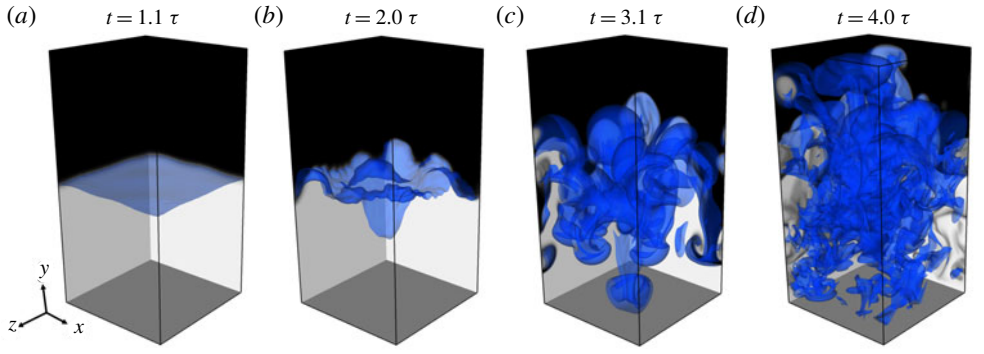


FIGURE 16. (Colour online) Evolution of mole fraction using the optimized perturbation amplitudes that maximize VAR. Same colour scheme as figure 2.

ensuring the average wavenumber components $k = \sqrt{k_x^2 + k_z^2}$ are approximately equal to the values obtained from the two-dimensional enhanced solution.

The evolution of the mole fraction using the interfacial perturbations that optimize VAR is shown in figure 16. It can immediately be seen that substantial mixing and penetration is achieved compared to the baseline solution over the same time horizon (see figure 2). Despite being initialized with the same perturbation energy in two dimensions, compared to the evolution in two dimensions (figure 15*e–h*), the flow exhibits three-dimensional behaviour as early as $t = 2\tau$, resulting in significantly more mixing compared to its two-dimensional counterpart. Figure 17 shows the conventional measures of mixing corresponding to the enhanced objective functions compared to the baseline case. Overall, significant increase in growth and mixing is observed. The objective functions are increased by factors of 1.7, 5.8 and 3.4 for MIX, KE and VAR, respectively, compared to the three-dimensional baseline case reported in § 4. Interestingly, greater enhancement is observed for two of the objective functions compared to the enhanced two-dimensional solutions, which were increased by factors of 1.4, 8.9 and 3.1 for MIX, KE and VAR, respectively. As shown in figures 17(*a*) and 17(*b*), the top and bottom walls act to decelerate the bubble heights and bubble tip velocities at later times. Thus, even greater enhancement might be achieved if a larger domain size was considered.

6. Conclusions

We have studied the role of interfacial perturbations on the evolution of a multi-mode Rayleigh–Taylor instability. The objective was to determine the extent to which the RT growth rate and mixing can be enhanced and suppressed through careful manipulation of the initial conditions. A discrete adjoint-based method was used to compute sensitivity of mixing and growth to the amplitudes of the initial fluid interface. To quantify RT growth and mixing, three objective functions, $\mathcal{J}$, are defined: (i) a mixing quantity based on the variance of fluid mole fraction (MIX), (ii) a kinetic energy norm based on the vertical velocity (KE) and (iii) an objective function based on the variations of the mole fraction with respect to the unperturbed initial state (VAR). These quantities are integrated in time through different stages of the RT instability.

First, a three-dimensional RT instability was considered with thirty-two perturbation modes and constant amplitude in each horizontal direction. Four main stages during

https://doi.org/10.1017/jfm.2019.532 Published online by Cambridge University Press

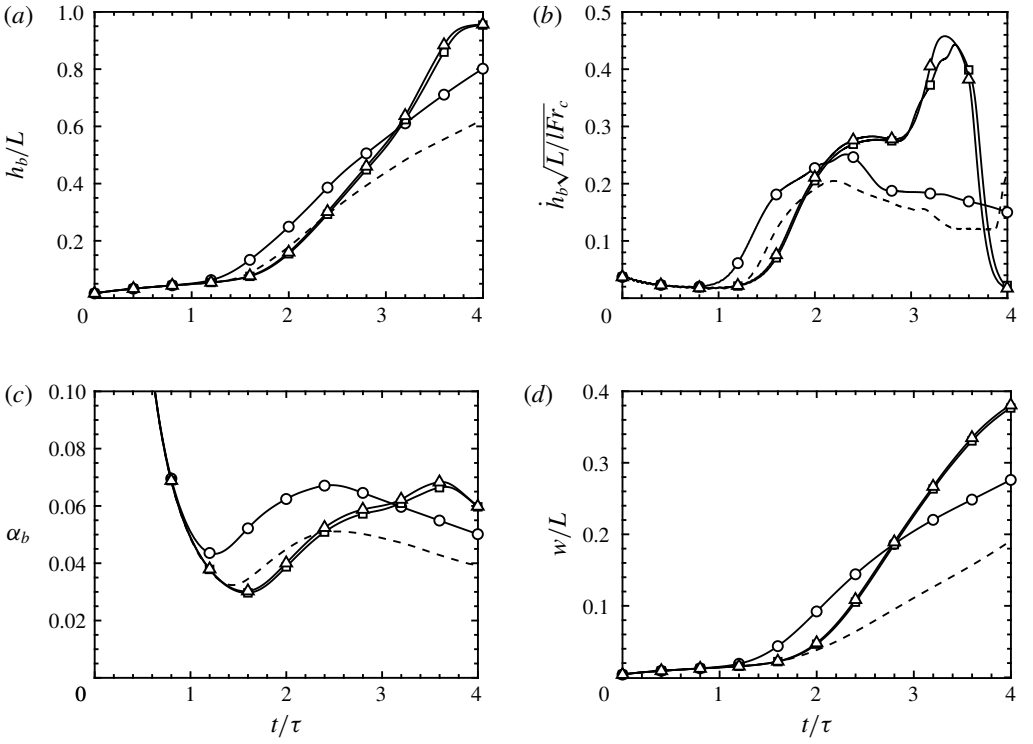


FIGURE 17. Evolution of (*a*) bubble height, (*b*) bubble tip velocity, (*c*) bubble growth parameter and (*d*) mixing width of the three-dimensional RT instabilities with the baseline case (– –) and with the initial interfacial perturbations of the enhanced two-dimensional RT instabilities of MIX (–○–), KE (–□–) and VAR (–△–).

RT growth are observed: a diffusion growth regime where molecular diffusion dominates, an exponential growth regime where the perturbations grow exponentially and the growth rate can be estimated by linear stability theory, a potential flow growth stage where nonlinearities become important and saturate the bubble tip velocity and a late-stage growth regime where self-similar RT growth ($h_b \propto t^2$) is observed. Except for the DG regime, the most sensitive wavenumber of each objective function approximately equals the most unstable wavenumber predicted by linear stability theory ($k \approx 8$). At early times, the spectrum of interfacial perturbations was found to differ between the different objective functions. However, they were found to collapse at later stages of the instability. It was found that randomly varying the phase distribution of initial perturbations can significantly alter both the growth rate and its sensitivity during the PFG and LSG stages. The sensitivity of the objective function to local mole fraction was also evaluated. Maximum sensitivity exists within the vicinity of the fluid interface, and becomes noisier as the integration time t_f increases. This is attributed to the chaotic behaviour of the instability, characterized by positive values of the first Lyapunov exponent associated with each objective function.

Sensitivity obtained from the adjoint solution is then used to suppress and enhance mixing of two-dimensional multi-mode RT instabilities. First, the objective functions are integrated over a duration $t_f = 4\tau$. The adjoint-based optimization approach was

https://doi.org/10.1017/jfm.2019.532 Published online by Cambridge University Press

capable of suppressing the instability by shifting all of the initial perturbation energy into the highest wavenumber modes. This result is supported by linear stability theory which predicts that initial perturbation amplitudes exponentially decay for $k > 21$. The optimal solutions for enhancing growth and mixing are less trivial. The optimization procedure was able to enhance MIX, KE and VAR relative to the baseline solution (uniform distributed perturbations) by 40 %, 300 % and 880 %, respectively. This corresponds to a maximum increase in the bubble growth parameter and mixing width by 32 % and 54 %, respectively. Initial perturbations of all mixing quantities demonstrate that low wavenumbers are favoured. The perturbation energy for wavenumber modes $k \gtrsim 20$ is eliminated, as anticipated by linear stability theory.

Enhancing RT growth and mixing over a shorter duration ($t_f = 2\tau$) was also studied. The majority of initial perturbation energy of the optimal solutions shifts towards the most unstable mode predicted by linear stability theory compared with the optimal perturbations when $t_f = 4\tau$. Comparing the optimized solutions for $t_f = 2\tau$ and $t_f = 4\tau$ yields two main conclusions: (i) lower wavenumber modes are more effective in enhancing growth for later times while the modes near the most unstable mode have greater effect in the linear and early nonlinear regimes; and (ii) due to the nonlinear, chaotic behaviour of RT instabilities at late stages of its growth, the optimal solution of early-time growth provides sub-optimal solutions at later times.

The adjoint-based optimization methodology used here demonstrates its capability to enhance and suppress mixing in unsteady multi-component flows. While it is well known that long time horizons can result in diverging adjoint sensitivities due to chaos (e.g. see Lea *et al.* 2000; Wang & Gao 2013), we demonstrate that the discrete adjoint approach provides useful sensitivity for optimizing mixing throughout the nonlinear RT regime, despite the existence of positive Lyapunov exponents. It was also shown that the optimized perturbations obtained from two-dimensional simulations admit similar (and sometimes better) improvement when imposed in three-dimensional configurations, making adjoint-based optimization particularly attractive for controlling large-scale unsteady flows. Such a technique can be extended to study the role of viscous and compressibility effects on the growth of fluid instabilities at late-time nonlinear stages. The utility of such an approach at even later stages must be addressed.

Acknowledgements

Computing resources were provided by the National Science Foundation via grant 1531752 MRI: Acquisition of Conflux, A Novel Platform for Data-Driven Computational Physics (Technical Monitor: E. Walker).

Appendix A. Continuous adjoint equations

In this appendix, the adjoint equations are derived for three-dimensional multi-component flows. As mentioned in § 3.3, the first line of (3.15) must vanish to exclude the variations of $\boldsymbol{Q}$ in $\delta\mathcal{J}$, leading to

$$\left(\frac{\partial \mathcal{I}}{\partial \boldsymbol{Q}}\right)^{\mathrm{T}} \delta\boldsymbol{Q}\mathcal{W} - \boldsymbol{Q}^{\dagger\mathrm{T}}\delta\boldsymbol{\mathcal{N}} - \boldsymbol{Q}^{\dagger\mathrm{T}}\delta\boldsymbol{Q}\delta_{t=0} = 0, \tag{A 1}$$

where $\delta\boldsymbol{\mathcal{N}}$ denotes variations of the governing equations (2.3)–(2.6) with respect to $\boldsymbol{Q}$, given by

$$\delta\mathcal{N}_1 = \frac{\partial \delta\rho}{\partial t} + \frac{\partial \delta\left(\rho u_j\right)}{\partial x_j}, \tag{A 2}$$

https://doi.org/10.1017/jfm.2019.532 Published online by Cambridge University Press

$$\delta\mathcal{N}_{i+1} = \frac{\partial\delta\left(\rho u_i\right)}{\partial t} + \frac{\partial}{\partial x_j}\left[u_j\delta(\rho u_i) + u_i\delta(\rho u_j) - u_i u_j\delta\rho + \delta p\delta_{ij} - \delta\tau_{ij}\right] + \frac{\delta\rho}{Fr_c}\delta_{2i}, \quad \text{for } i = 1, 2, 3, \tag{A 3}$$

$$\delta\mathcal{N}_5 = \frac{\partial\delta\left(\rho E\right)}{\partial t} + \frac{\partial}{\partial x_j}\left\{\left[\delta(\rho E) + \delta p\right]u_j + \left(E + \frac{p}{\rho}\right)\left[\delta(\rho u_j) - u_j\delta\rho\right] + \delta q_j - u_i\delta\tau_{ij} - \frac{\tau_{ij}}{\rho}\left[\delta(\rho u_i) - u_i\delta\rho\right]\right\} + \frac{\delta(\rho u_2)}{Fr_c}, \tag{A 4}$$

$$\delta\mathcal{N}_6 = \frac{\partial\delta\left(\rho Y\right)}{\partial t} + \frac{\partial}{\partial x_j}\left[Y\delta(\rho u_j) + u_j\delta(\rho Y) - u_j Y\delta\rho\right] - \frac{1}{Re_c Sc}\frac{\partial^2}{\partial x_j\partial x_j}\left\{\frac{1}{\rho}\left[\delta(\rho Y) - Y\delta\rho\right]\right\}, \tag{A 5}$$

where δp, $\delta\tau_{ij}$ and δq_i can be determined according to (2.7), (2.8) and (2.9), respectively, which yields

$$\delta p = (\gamma - 1)\left[\delta(\rho E) - u_i\delta(\rho u_i) + \frac{u_i u_i}{2}\delta\rho\right], \tag{A 6}$$

$$\delta\tau_{ij} = \frac{1}{Re_c}\left[\frac{\partial}{\partial x_j}\left\{\frac{1}{\rho}\left[\delta(\rho u_i) - u_i\delta\rho\right]\right\} + \frac{\partial}{\partial x_i}\left\{\frac{1}{\rho}\left[\delta(\rho u_j) - u_j\delta\rho\right]\right\} - \frac{2}{3}\frac{\partial}{\partial x_k}\left\{\frac{1}{\rho}\left[\delta(\rho u_k) - u_k\delta\rho\right]\right\}\delta_{ij}\right], \tag{A 7}$$

$$\delta q_i = -\frac{1}{Re_c Pr}\frac{\partial\delta T}{\partial x_i} - \frac{1}{Re_c Sc\widehat{W}}\left[\delta T\frac{\partial Y}{\partial x_i} + T\frac{\partial}{\partial x_i}\left\{\frac{1}{\rho}\left[\delta(\rho Y) - Y\delta\rho\right]\right\}\right], \tag{A 8}$$

where $\widehat{W} = (W_2^{-1} - W_1^{-1})^{-1}$, and δT is obtained using (2.10), given by

$$\frac{\delta T}{T} = \frac{\delta p}{p} + \frac{\delta\overline{W}}{\overline{W}} - \frac{\delta\rho}{\rho}, \tag{A 9}$$

with

$$\frac{\delta\overline{W}}{\overline{W}} = -\frac{\overline{W}}{\rho\widehat{W}}\left[\delta(\rho Y) - Y\delta\rho\right], \tag{A 10}$$

according to (2.11). Substituting $\delta\mathcal{N}$ from (A 2)–(A 5) into (A 1), employing integration by parts and decomposing each component of $\delta\boldsymbol{Q}$ yields the following adjoint equations

$$\begin{aligned}
&\partial_t\rho^\dagger + \left[-u_i u_j + \phi^2\delta_{ij}\right]\partial_j u_i^\dagger - (3\rho Re_c)^{-1}\left(3u_i\partial_{jj}^2 u_i^\dagger + u_j\partial_{ij}^2 u_i^\dagger\right) \\
&- Fr_c^{-1}v^\dagger + \left(-Eu_j + \phi^2 u_j - pu_j/\rho + u_i\tau_{ij}/\rho\right)\partial_j E^\dagger \\
&- (3\rho Re_c)^{-1}\left[3u_i\partial_j(u_i\partial_j E^\dagger) + 3u_j\partial_i(u_i\partial_j E^\dagger) - 2u_i\partial_i(u_j\partial_j E^\dagger)\right] \\
&+ T(\rho Re_c)^{-1}\left(\phi^2\rho p^{-1} + Y\overline{W}\widehat{W}^{-1} - 1\right)\left(Pr^{-1}\partial_{jj}^2 E^\dagger - Sc^{-1}\widehat{W}^{-1}\partial_j Y\partial_j E^\dagger\right) \\
&- Y(\rho Re_c Sc\widehat{W})^{-1}\partial_j\left(T\partial_j E^\dagger\right) - u_j Y\partial_j Y^\dagger - Y(\rho Re_c Sc)^{-1}\partial_{jj}^2 Y^\dagger + \frac{\partial\mathcal{I}}{\partial\rho}\mathcal{W} = 0,
\end{aligned} \tag{A 11}$$

https://doi.org/10.1017/jfm.2019.532 Published online by Cambridge University Press

$$\begin{aligned}
&\partial_t u_i^\dagger + \partial_i \rho^\dagger + u_j \partial_j u_i^\dagger + u_j \partial_i u_j^\dagger - (\gamma-1) u_i \partial_j u_j^\dagger - Fr_c^{-1} E^\dagger \delta_{2i} \\
&+ (3\rho Re_c)^{-1} \left(3\partial_{jj}^2 u_i^\dagger + \partial_{ij}^2 u_j^\dagger\right) - \left[(\gamma-1) u_i u_j + \tau_{ij}\rho^{-1}\right] \partial_j E^\dagger \\
&+ (3\rho Re_c)^{-1} \left[3\partial_j \left(u_i \partial_j E^\dagger\right) + 3\partial_j \left(u_j \partial_i E^\dagger\right) - 2\partial_i \left(u_j \partial_j E^\dagger\right)\right] \\
&+ \gamma \overline{W} u_i \left(\rho Re_c\right)^{-1} \left(Sc^{-1} \widehat{W}^{-1} \partial_j Y \partial_j E^\dagger - Pr^{-1} \partial_{jj}^2 E^\dagger\right) \\
&+ \left(E + \rho^{-1} p\right) \partial_i E^\dagger + Y \partial_i Y^\dagger + \frac{\partial \mathcal{I}}{\partial \rho u_i} \mathcal{W} = 0,
\end{aligned} \tag{A 12}$$

$$\begin{aligned}
&\partial_t E^\dagger + \gamma \overline{W} \left(\rho Re_c\right)^{-1} \left(Pr^{-1} \partial_{jj}^2 E^\dagger - Sc^{-1} \widehat{W}^{-1} \partial_j Y \partial_j E^\dagger\right) \\
&+ (\gamma-1) \partial_i u_i^\dagger + \gamma u_j \partial_j E^\dagger + \frac{\partial \mathcal{I}}{\partial \rho E} \mathcal{W} = 0,
\end{aligned} \tag{A 13}$$

$$\begin{aligned}
&\partial_t Y^\dagger + u_j \partial_j Y^\dagger + \left(\rho Re_c Sc\right)^{-1} \partial_{jj}^2 Y^\dagger + \left(\rho Re_c Sc \widehat{W}\right)^{-1} \partial_j \left(T \partial_j E^\dagger\right) \\
&+ T \overline{W} \left(\rho Re_c \widehat{W}\right)^{-1} \left(Sc^{-1} \widehat{W}^{-1} \partial_j Y \partial_j E^\dagger - Pr^{-1} \partial_{jj}^2 E^\dagger\right) + \frac{\partial \mathcal{I}}{\partial \rho Y} \mathcal{W} = 0,
\end{aligned} \tag{A 14}$$

where $\partial_t = \partial/\partial t$ and $\partial_i = \partial/\partial x_i$ are used for brevity, and $\phi^2 = (\gamma-1) u_i u_i / 2$.

Appendix B. Theoretical estimates of early-time sensitivity

In § 4.2, the adjoint sensitivities of mixing and growth to initial interfacial perturbations were reported for different stages of the RT instability. In this appendix, we employ established theories that describe the early-time RT growth rates to estimate sensitivity and compare with the adjoint solutions. During the DG regime, the flow is dominated by molecular diffusion. During the diffusion dominated regime, the diffusion thickness broadens according to $\sqrt{\delta_D^2 + 4Dt}$ (Duff *et al.* 1962; Cook & Dimotakis 2001). In addition, the amplitude of an initial perturbation with wavenumber k at the interface decays in time with an exponential rate of $-k^2 D$ (Duff *et al.* 1962). With this, the mole fraction evolution in a diffusion dominated flow can be expressed as

$$X(x, y, z, t) \approx \frac{1}{2} \left\{ 1 + \operatorname{erf} \left[\frac{y - h(x, z, t)}{\sqrt{\delta_D^2 + 4Dt}} \right] \right\}, \tag{B 1}$$

where the evolution of the interface is

$$h(x, z, t) = \sum_{m=1}^{M} \sum_{n=1}^{N} A_{m,n} \cos\left(k_{x,m} x + \theta_{x,m}\right) \cos\left(k_{z,n} z + \theta_{z,n}\right) \exp\left(\sigma_{m,n} t\right). \tag{B 2}$$

The interfacial growth rate during the diffusion regime is given by

$$\sigma_{m,n}^{(DG)} = -D(k_{x,m}^2 + k_{z,n}^2), \tag{B 3}$$

where $k_{x,m}$ and $k_{z,n}$ are wavenumbers in the x and z-directions, respectively.

https://doi.org/10.1017/jfm.2019.532 Published online by Cambridge University Press

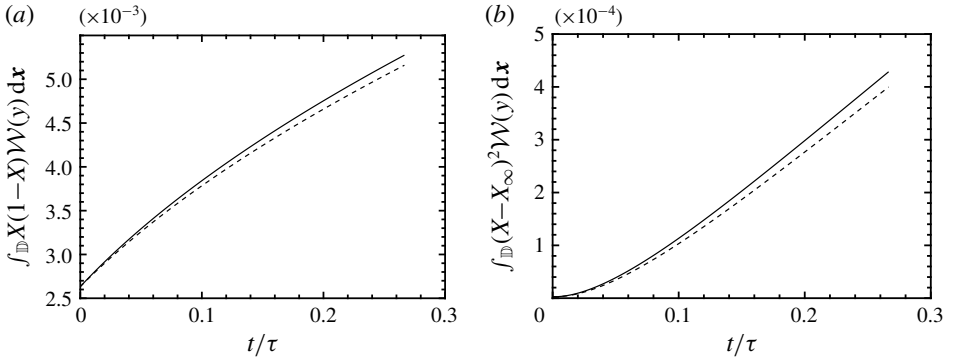


FIGURE 18. Temporal evolution of the objective functions of a three-dimensional multi-mode RT instability from the simulation (–) and the model given by (B 1) (– –).

Figure 18 compares the integral of $\mathcal{I}\mathcal{W}(y)$ over the entire domain from the numerical simulations and the model (B 1) for both MIX and VAR. As can be seen, the model solution deviates from the simulation with increasing t. As time increases, the inertial effects of the fluid become more important due to buoyancy, and in this regime, the diffusion model approximation is less robust at capturing these effects. However, as can be seen, the model provides an excellent approximation of the objective functions when $t < 0.2\tau$.

Recalling (3.10), the sensitivity of VAR is obtained by taking its derivative with respect to the initial interfacial amplitudes, given by

$$\frac{\delta \mathcal{J}}{\delta A_{m,n}} = \int_0^{t_f} \int_{\mathbb{D}} 2 \frac{\delta X}{\delta A_{m,n}} \left(X - X_\infty\right) \mathcal{W}(y) \, \mathrm{d}\boldsymbol{x} \, \mathrm{d}t, \quad \text{for } \mathcal{J} = \mathrm{VAR}, \tag{B 4}$$

where $\delta X/\delta A_{mn}$ is derived according to (B 1) and (B 2), which yields

$$\frac{\delta X}{\delta A_{m,n}} \approx -\frac{\cos\left(k_{x,m}x + \theta_{x,m}\right) \cos\left(k_{z,n}z + \theta_{z,n}\right)}{\sqrt{\pi\left(\delta_D^2 + 4Dt\right)}} \exp\left\{-\frac{\left[y - h(x,z)\right]^2}{\delta_D^2 + 4Dt} + \sigma_{m,n}^{(DG)} t\right\}. \tag{B 5}$$

The VAR sensitivities computed by substituting (B 1) and (B 5) into (B 4) are compared with the adjoint sensitivity for early-time durations (see figure 19*a*). The sensitivity predicted by the model closely matches the adjoint-based sensitivity at early times and deviates at later times. This effect is more evident at low wavenumbers since they have more substantial growth in the EG regime according to (4.1). In order to include the fluid inertial effects in the model, the diffusion growth rate of the interface $\sigma^{(DG)}$ in (B 2) can be replaced by the exponential growth rate predicted by linear stability theory, i.e. $\sigma^{(EG)}$ given by (4.1) (see figure 19*b*). Even with these simplifications, the model is able to predict the trends in sensitivity with respect to wavenumber reasonably well.

Similarly, the sensitivity of MIX is obtained by taking derivatives of (3.8) with respect to initial interfacial amplitudes, given by

$$\frac{\delta \mathcal{J}}{\delta A_{m,n}} = \int_0^{t_f} \int_{\mathbb{D}} \frac{\delta X}{\delta A_{m,n}} \left(1 - 2X\right) \mathcal{W}(y) \, \mathrm{d}\boldsymbol{x} \, \mathrm{d}t, \quad \text{for } \mathcal{J} = \mathrm{MIX}, \tag{B 6}$$

https://doi.org/10.1017/jfm.2019.532 Published online by Cambridge University Press

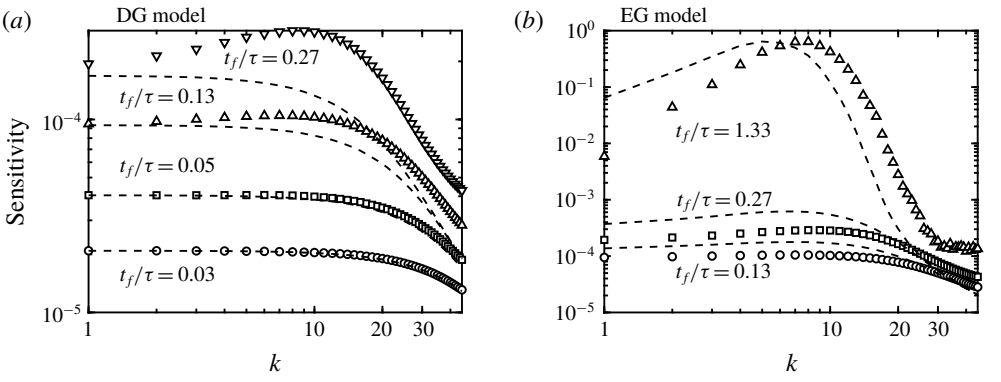


FIGURE 19. Magnitude of VAR sensitivity $|\delta\mathcal{J}/\delta\boldsymbol{A}|$ integrated over different durations t_f from adjoint simulations (symbols) and the model given by (B 5) (−−) with the growth rate applicable to (*a*) the DG regime, i.e. (B 3) and (*b*) the EG regime, i.e. (4.1). The sensitivities are shown as a function of initial perturbation wavenumber $k = \sqrt{k_x^2 + k_z^2}$.

where $\delta X/\delta A_{mn}$ is given by (B 5). However, directly employing the model described in (B 1) results in zero sensitivity. This can be shown by substituting (B 1) and (B 5) into (B 6) and rearranging, giving

$$\frac{\delta\mathcal{J}}{\delta A_{m,n}} = \int_{t=0}^{t_f} \exp\left[-D(k_{x,m}^2 + k_{z,n}^2)t\right] \int_{x=-\pi}^{\pi} \cos\left(k_{x,m}x + \theta_{x,m}\right) \int_{z=-\pi}^{\pi} \cos\left(k_{z,n}z + \theta_{z,n}\right) \times \int_{y'=(-2\pi-h)/\sqrt{\delta_D^2+4Dt}}^{(2\pi-h)/\sqrt{\delta_D^2+4Dt}} \exp(-y'^2)\,\mathrm{erf}(y')\mathcal{W}(y'\Delta(t) + h(x,z,t))\,\mathrm{d}y'\,\mathrm{d}z\,\mathrm{d}x\,\mathrm{d}t, \quad \text{for } \mathcal{J} = \mathrm{MIX}, \tag{B 7}$$

where $y' = y - h(x, z, t)/\sqrt{\delta_D^2 + 4Dt}$. Since h is sufficiently small at early times, the integrand reduces to an odd function with respect to y'. Due to the symmetry of the domain, the resulting integral is null. Alternatively, the sensitivity can be provided via a numerical solution to the following diffusion equation

$$\frac{\partial X}{\partial t} = D\frac{\partial^2 X}{\partial x_i \partial x_i}, \tag{B 8}$$

where D denotes the mass diffusivity. This is derived by neglecting fluid inertia and taking the density and molecular weight of the mixture to be constant in (2.6). As shown in figure 20, the resulting sensitivity obtained by solving (B 8) closely matches the adjoint solution. The small differences can be related to assumptions of constant density, diffusivity and molecular weight, and neglecting inertial forces and gravity effects.

It is also possible to find an estimate for the sensitivity of KE with respect to k. Assuming the dominant vertical velocity at early time is located at the interface, the objective function can be rewritten as

$$\mathrm{KE} = \int_0^{t_f} \int_{\mathbb{D}} v^2 \mathcal{W}(y)\,\mathrm{d}\boldsymbol{x}\,\mathrm{d}t \propto \int_0^{t_f} \int_{\mathbb{D}} \left(\frac{\mathrm{d}h}{\mathrm{d}t}\right)^2 \mathcal{W}(y)\,\mathrm{d}\boldsymbol{x}\,\mathrm{d}t. \tag{B 9}$$

https://doi.org/10.1017/jfm.2019.532 Published online by Cambridge University Press

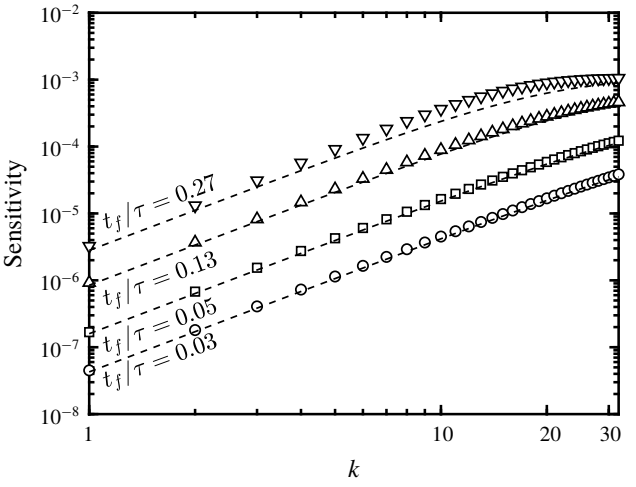


FIGURE 20. Sensitivity $\delta\mathcal{J}/\delta\boldsymbol{A}$ for $\mathcal{J} = \text{MIX}$ integrated over different durations t_f from adjoint simulations (symbols) and model (– –) obtained by (B 6).

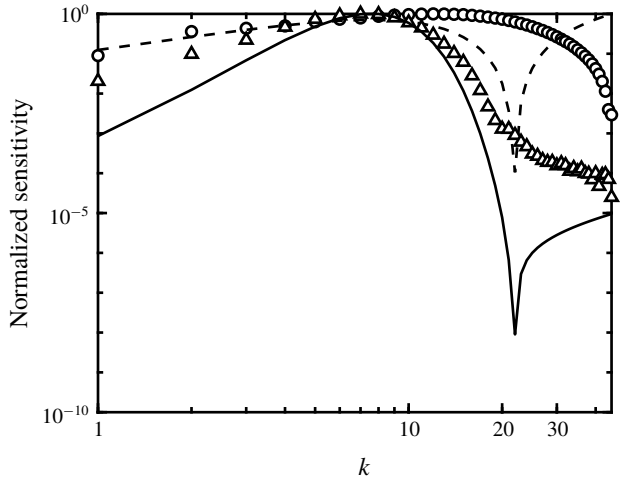


FIGURE 21. Magnitude of sensitivity $|\delta\mathcal{J}/\delta\boldsymbol{A}|$ for $\mathcal{J} = \text{KE}$ integrated over different durations, $t_f = 0.13\tau$ from simulation (○) and (B 10) (– –) and $t_f = 1.33\tau$ from simulation (△) and (B 10) (–). The sensitivities are shown as a function of initial perturbation wavenumber $k = \sqrt{k_x^2 + k_z^2}$ and normalized by their corresponding maximum value.

Substituting (B 2) into (B 9) and taking the derivative with respect to $A_{m,n}$ yields

$$\frac{\delta\mathcal{J}}{\delta A_{m,n}} \propto A_{m,n}\sigma_{m,n}^{(EG)}\left[\exp\left(2\sigma_{m,n}^{(EG)}t_f\right) - 1\right], \quad \text{for } \mathcal{J} = \text{KE}, \tag{B 10}$$

where the growth rate is estimated from linear stability theory. In (B 9), $\sigma_{m,n}^{(EG)}$ is taken to be time independent even though the EG growth rate (4.1) might vary with time according to Duff *et al.* (1962). As can be seen in figure 21, the model is able to predict the sensitivity behaviour with respect to wavenumber. The differences between

https://doi.org/10.1017/jfm.2019.532 Published online by Cambridge University Press

the adjoint sensitivities and the model is attributed to neglecting velocities farther from the interface and also from any errors that might arise in (4.1).

REFERENCES

AAMO, O. M., KRSTIĆ, M. & BEWLEY, T. R. 2003 Control of mixing by boundary feedback in 2D channel flow. *Automatica* **39** (9), 1597–1606.

ALON, U., HECHT, J., MUKAMEL, D. & SHVARTS, D. 1994 Scale invariant mixing rates of hydrodynamically unstable interfaces. *Phys. Rev. Lett.* **72** (18), 2867–2870.

ANUCHINA, N. N., KUCHERENKO, Y. A., NEUVAZHAEV, V. E., OGIBINA, V. N., SHIBARSHOV, L. I. & YAKOVLEV, V. G. 1978 Turbulent mixing at an accelerating interface between liquids of different density. *Fluid Dyn.* **13** (6), 916–920.

BABCHIN, A. J., FRENKEL, A. L., LEVICH, B. G. & SIVASHINSKY, G. I. 1983 Nonlinear saturation of Rayleigh–Taylor instability in thin films. *Phys. Fluids* **26** (11), 3159–3161.

BAKER, L. & FREEMAN, J. R. 1981 Heuristic model of the nonlinear Rayleigh–Taylor instability. *J. Appl. Phys.* **52** (2), 655–663.

BANERJEE, A. & ANDREWS, M. J. 2009 3D simulations to investigate initial condition effects on the growth of Rayleigh–Taylor mixing. *Intl J. Heat Mass Transfer* **52** (17), 3906–3917.

BODONY, D. J. 2010 Accuracy of the simultaneous-approximation-term boundary condition for time-dependent problems. *J. Sci. Comput.* **43** (1), 118–133.

BRAMAN, K., OLIVER, T. A. & RAMAN, V. 2015 Adjoint-based sensitivity analysis of flames. *Combust. Theor. Model.* **19** (1), 29–56.

CABOT, W. 2006 Comparison of two-and three-dimensional simulations of miscible Rayleigh–Taylor instability. *Phys. Fluids* **18** (4), 045101.

CABOT, W. H. & COOK, A. W. 2006 Reynolds number effects on Rayleigh–Taylor instability with possible implications for type Ia supernovae. *Nat. Phys.* **2** (8), 562–568.

CAPECELATRO, J., BODONY, D. J. & FREUND, J. B. 2017 Adjoint-based sensitivity analysis of ignition in a turbulent reactive shear layer. In *55th AIAA Aerospace Sciences Meeting, AIAA* 2017-0846. AIAA.

CAPECELATRO, J., BODONY, D. J. & FREUND, J. B. 2018 Adjoint-based sensitivity and ignition threshold mapping in a turbulent mixing layer. *Combust. Theor. Model.* 147–179.

CAPECELATRO, J., VISHNAMPET, R., BODONY, D. J. & FREUND, J. B. 2016 Adjoint-based sensitivity analysis of localized ignition in a non-premixed hydrogen-air mixing layer. In *54th AIAA Aerospace Sciences Meeting, AIAA* 2016-2153. AIAA.

CARLES, P., HUANG, Z., CARBONE, G. & ROSENBLATT, C. 2006 Rayleigh–Taylor instability for immiscible fluids of arbitrary viscosities: a magnetic levitation investigation and theoretical model. *Phys. Rev. Lett.* **96** (10), 104501.

CARNARIUS, A., THIELE, F., OEZKAYA, E. & GAUGER, N. R. 2010 Adjoint approaches for optimal flow control. *AIAA Paper* 2010-5088.

CARPENTER, M. H., GOTTLIEB, D. & ABARBANEL, S. 1994 Time-stable boundary conditions for finite-difference schemes solving hyperbolic systems: methodology and application to high-order compact schemes. *J. Comput. Phys.* **111** (2), 220–236.

CHANDRASEKHAR, S. 1961 Hydrodynamic and hydromagnetic stability. In *International Series of Monographs on Physics*. Clarendon Press.

CIMPEANU, R., PAPAGEORGIOU, D. T. & PETROPOULOS, P. G. 2014 On the control and suppression of the Rayleigh–Taylor instability using electric fields. *Phys. Fluids* **26** (2), 022105.

COOK, A. W. 2009 Enthalpy diffusion in multicomponent flows. *Phys. Fluids* **21** (5), 055109.

COOK, A. W. & DIMOTAKIS, P. E. 2001 Transition stages of Rayleigh–Taylor instability between miscible fluids. *J. Fluid Mech.* **443**, 69–99.

DIMONTE, G. 2004 Dependence of turbulent Rayleigh–Taylor instability on initial perturbations. *Phys. Rev.* E **69** (5), 056305.

DIMONTE, G., YOUNGS, D. L., DIMITS, A., WEBER, S., MARINAK, M., WUNSCH, S., GARASI, C., ROBINSON, A., ANDREWS, M. J., RAMAPRABHU, P. *et al.* 2004 A comparative study of

https://doi.org/10.1017/jfm.2019.532 Published online by Cambridge University Press

the turbulent Rayleigh–Taylor instability using high-resolution three-dimensional numerical simulations: the Alpha-Group collaboration. *Phys. Fluids* **16** (5), 1668–1693.

DUFF, R. E., HARLOW, F. H. & HIRT, C. W. 1962 Effects of diffusion on interface instability between gases. *Phys. Fluids* **5** (4), 417–425.

FOURES, D. P. G., CAULFIELD, C. P. & SCHMID, P. J. 2014 Optimal mixing in two-dimensional plane Poiseuille flow at finite Péclet number. *J. Fluid Mech.* **748**, 241–277.

FREUND, J. B. 1997 Proposed inflow/outflow boundary condition for direct computation of aerodynamic sound. *AIAA J.* **35** (4), 740–742.

FUJIMOTO, M. Y. 1993 The evolution of accreting stars with turbulent mixing. *Astrophys. J.* **419**, 768–775.

GONCHAROV, V. N. 2002 Analytical model of nonlinear, single-mode, classical Rayleigh–Taylor instability at arbitrary Atwood numbers. *Phys. Rev. Lett.* **88** (13), 134502.

HAAN, S. W. 1989 Onset of nonlinear saturation for Rayleigh–Taylor growth in the presence of a full spectrum of modes. *Phys. Rev.* A **39** (11), 5812–5825.

HALPERN, D. & FRENKEL, A. L. 2001 Saturated Rayleigh–Taylor instability of an oscillating Couette film flow. *J. Fluid Mech.* **446**, 67–93.

HECHT, J., ALON, U. & SHVARTS, D. 1994 Potential flow models of Rayleigh–Taylor and Richtmyer–Meshkov bubble fronts. *Phys. Fluids* **6** (12), 4019–4030.

HUANG, Z., DE LUCA, A., ATHERTON, T. J., BIRD, M., ROSENBLATT, C. & CARLÈS, P. 2007 Rayleigh–Taylor instability experiments with precise and arbitrary control of the initial interface shape. *Phys. Rev. Lett.* **99** (20), 204502.

JAMESON, A. 1989 Aerodynamic design via control theory. In *Recent Advances in Computational Fluid Dynamics*, pp. 377–401. Springer.

JAMESON, A. & MARTINELLI, L. 2000 Aerodynamic shape optimization techniques based on control theory. In *Computational Mathematics Driven by Industrial Problems*, pp. 151–221. Springer.

JANKA, H.-T. & MÜLLER, E. 1996 Neutrino heating, convection, and the mechanism of type-II supernova explosions. *Astron. Astrophys.* **306**, 167–198.

JONES, E., OLIPHANT, T. & PETERSON, P. 2001 SciPy: Open source scientific tools for Python. http://www.scipy.org/.

KRAFT, D. 1988 A software package for sequential quadratic programming. *Forschungsbericht-Deutsche Forschungs- und Versuchsanstalt fur Luft- und Raumfahrt*.

KREISS, H.-O. & SCHERER, G. 1974 Finite element and finite difference methods for hyperbolic partial differential equations. In *Mathematical Aspects of Finite Elements in Partial Differential Equations*, pp. 195–212. Elsevier.

LAYZER, D. 1955 On the instability of superposed fluids in a gravitational field. *Astrophys. J.* **122**, 1–12.

LEA, D. J., ALLEN, M. R. & HAINE, T. W. N. 2000 Sensitivity analysis of the climate of a chaotic system. *Tellus* A **52** (5), 523–532.

LINDL, J. 1995 Development of the indirect-drive approach to inertial confinement fusion and the target physics basis for ignition and gain. *Phys. Plasmas* **2** (11), 3933–4024.

LIU, W. 2006 Mixing enhancement via flow optimization. In *Decision and Control, 2006 45th IEEE Conference on*, pp. 5323–5328. IEEE.

LIVESCU, D. 2004 Compressibility effects on the Rayleigh–Taylor instability growth between immiscible fluids. *Phys. Fluids* **16** (1), 118–127.

LIVESCU, D. 2013 Numerical simulations of two-fluid turbulent mixing at large density ratios and applications to the Rayleigh–Taylor instability. *Phil. Trans. R. Soc. Lond.* A **371** (2003), 20120185.

LIVESCU, D., WEI, T. & PETERSEN, M. R. 2011 Direct numerical simulations of Rayleigh–Taylor instability. In *J. Phys: Conference Series, vol. 318*, p. 082007. IOP Publishing.

LOPEZ-ZAZUETA, A., FONTANE, J. & JOLY, L. 2016 Optimal perturbations in time-dependent variable-density Kelvin–Helmholtz billows. *J. Fluid Mech.* **803**, 466–501.

MARTINS, J. R. R. A., ALONSO, J. J. & REUTHER, J. J. 2004 High-fidelity aerostructural design optimization of a supersonic business jet. *J. Aircraft* **41** (3), 523–530.

https://doi.org/10.1017/jfm.2019.532 Published online by Cambridge University Press

MATTSSON, K., SVÄRD, M. & NORDSTRÖM, J. 2004 Stable and accurate artificial dissipation. *J. Sci. Comput.* **21** (1), 57–79.

MILES, C. J. 2018 Optimal control of the advection-diffusion equation for effective fluid mixing. PhD thesis, University of Michigan, Ann Arbor, MI.

MILLMAN, K. J. & AIVAZIS, M. 2011 Python for scientists and engineers. *Comput. Sci. & Engng* **13** (2), 9–12.

MOVAHED, P. 2014 High-fidelity numerical simulations of compressible turbulence and mixing generated by hydrodynamic instabilities. PhD thesis, University of Michigan, Ann Arbor, MI.

NADARAJAH, S. & JAMESON, A. 2000. A comparison of the continuous and discrete adjoint approach to automatic aerodynamic optimization. *AIAA Paper* 2000-0667.

NAKAI, S. & TAKABE, H. 1996 Principles of inertial confinement fusion-physics of implosion and the concept of inertial fusion energy. *Rep. Prog. Phys.* **59** (9), 1071–1131.

OLIPHANT, T. E. 2007 Python for scientific computing. *Comput. Sci. Engng* **9** (3), 10–20.

ORON, D., ARAZI, L., KARTOON, D., RIKANATI, A., ALON, U. & SHVARTS, D. 2001 Dimensionality dependence of the Rayleigh–Taylor and Richtmyer–Meshkov instability late-time scaling laws. *Phys. Plasmas* **8** (6), 2883–2889.

PETERS, N. 2000 *Turbulent Combustion*. Cambridge University Press.

PIRO, A. L. & BILDSTEN, L. 2007 Turbulent mixing in the surface layers of accreting neutron stars. *Astrophys. J.* **663** (2), 1252–1268.

PITSCH, H. 2006 Large-eddy simulation of turbulent combustion. *Annu. Rev. Fluid Mech.* **38**, 453–482.

QADRI, U. A., CHANDLER, G. J. & JUNIPER, M. P. 2015 Self-sustained hydrodynamic oscillations in lifted jet diffusion flames: origin and control. *J. Fluid Mech.* **775**, 201–222.

RAMAPRABHU, P., DIMONTE, G. & ANDREWS, M. J. 2005 A numerical study of the influence of initial perturbations on the turbulent Rayleigh–Taylor instability. *J. Fluid Mech.* **536**, 285–319.

READ, K. I. 1984 Experimental investigation of turbulent mixing by Rayleigh–Taylor instability. *Physica* D **12** (1-3), 45–58.

RECKINGER, S. J., LIVESCU, D. & VASILYEV, O. V. 2016 Comprehensive numerical methodology for direct numerical simulations of compressible Rayleigh–Taylor instability. *J. Comput. Phys.* **313**, 181–208.

RISTORCELLI, J. R. & CLARK, T. T. 2004 Rayleigh–Taylor turbulence: self-similar analysis and direct numerical simulations. *J. Fluid Mech.* **507**, 213–253.

ROBERTS, M. S. & JACOBS, J. W. 2016 The effects of forced small-wavelength, finite-bandwidth initial perturbations and miscibility on the turbulent Rayleigh–Taylor instability. *J. Fluid Mech.* **787**, 50–83.

SHARP, D. H. 1984 An overview of Rayleigh–Taylor instability. *Physica* D **12** (1), 3–18.

STRAND, B. 1994 Summation by parts for finite difference approximations for d/dx. *J. Comput. Phys.* **110** (1), 47–67.

SVÄRD, M. & NORDSTRÖM, J. 2008 A stable high-order finite difference scheme for the compressible Navier–Stokes equations: no-slip wall boundary conditions. *J. Comput. Phys.* **227** (10), 4805–4824.

THIFFEAULT, J.-L. 2012 Using multiscale norms to quantify mixing and transport. *Nonlinearity* **25** (2), R1.

TREVISAN, A. & LEGNANI, R. 1995 Transient error growth and local predictability: a study in the Lorenz system. *Tellus* A **47** (1), 103–117.

VERMACH, L. & CAULFIELD, C. P. 2018 Optimal mixing in three-dimensional plane Poiseuille flow at high Péclet number. *J. Fluid Mech.* **850**, 875–923.

VIKHANSKY, A. 2002 Enhancement of laminar mixing by optimal control methods. *Chem. Engng Sci.* **57** (14), 2719–2725.

VISHNAMPET, R., BODONY, D. J. & FREUND, J. B. 2015 A practical discrete-adjoint method for high-fidelity compressible turbulence simulations. *J. Comput. Phys.* **285**, 173–192.

VISHNAMPET GANAPATHI SUBRAMANIAN, R. 2015 An exact and consistent adjoint method for high-fidelity discretization of the compressible flow equations. PhD thesis, University of Illinois at Urbana-Champaign.

https://doi.org/10.1017/jfm.2019.532 Published online by Cambridge University Press

WANG, Q. & GAO, J.-H. 2013 The drag-adjoint field of a circular cylinder wake at Reynolds numbers 20, 100 and 500. *J. Fluid Mech.* **730**, 145–161.

WEI, M. & FREUND, J. B. 2006 A noise-controlled free shear flow. *J. Fluid Mech.* **546**, 123–152.

WEI, T. & LIVESCU, D. 2012 Late-time quadratic growth in single-mode Rayleigh–Taylor instability. *Phys. Rev.* E **86** (4), 046405.

WOOSLEY, S. E. & WEAVER, T. A. 1986 The physics of supernova explosions. *Annu. Rev. Astron. Astrophys.* **24** (1), 205–253.

XIE, C. Y., TAO, J. J., SUN, Z. L. & LI, J. 2017 Retarding viscous Rayleigh–Taylor mixing by an optimized additional mode. *Phys. Rev.* E **95** (2), 023109.

YOUNGS, D. L. 1984 Numerical simulation of turbulent mixing by Rayleigh–Taylor instability. *Physica D* **12** (1–3), 32–44.

YOUNGS, D. L. 2003 Application of miles to Rayleigh–Taylor and Richtmyer–Meshkov mixing. *AIAA Paper* 2003-4102.

YOUNGS, D. L. 2009 Application of monotone integrated large eddy simulation to Rayleigh–Taylor mixing. *Phil. Trans. R. Soc. Lond.* A **367** (1899), 2971–2983.

https://doi.org/10.1017/jfm.2019.532 Published online by Cambridge University Press